THREE–DIMENSIONAL HYDRODYNAMICS ON FINITE ELEMENTS. PART I: LINEARIZED HARMONIC MODEL

DANIEL R. LYNCH AND FRANCISCO E. WERNER

Thayer School of Engineering, Dartmouth College, Hanover, NH 03755, U.S.A.

SUMMARY

The linearized three-dimensional hydrodynamic equations are solved numerically for periodic motions, subject to a linear slip condition at the bottom. The structure of the linearized equations allows an exact uncoupling of the horizontal and vertical computations, so that they may be achieved sequentially rather than simultaneously, and without iteration. The solution strategy involves simple horizontal C^0 finite elements for the description of free surface elevation. Vertical variations in velocity may be treated analytically for some special variations of viscosity with depth; more generally the finite element method is employed with one-dimensional linear elements. Because of the uncoupling, the entire three-dimensional solution scales as a two-dimensional vertically averaged problem. The limiting two-dimensional problem may be solved as a Helmholtz-type problem for elevation alone, using established techniques.

Solutions for test problems are compared with known analytic solutions. Some simple gridding rules are established for the vertical discretization. Finally, a field application is shown involving the tidal response of the Lake Maracaibo (Venezuela) system.

INTRODUCTION

This paper deals with the fluid mechanics of large estuaries and coastal regions, and in particular with the large-scale, horizontal motions forced by wind and tide. In nearly all practical applications the naturally occurring geometry (both lateral boundaries and the bathymetric profile) exerts major influences on the motion. Thus useful models must resolve arbitrary geometry readily. This is a natural strength of the finite element method and we seek here to establish its validity and cost-effectiveness.

Effective two-dimensional harmonic solutions have been demonstrated by Pearson and Winter,[1] Le Provost and Poncet,[2] Jamart and Winter,[3] Walters[4] and Lynch.[5,6] In these applications the vertically averaged equations are solved with the bottom stress represented in terms of the vertically averaged velocity. In reality a significant discrepancy can exist between these two quantities, both in timing and in direction. Hence, the need arises for full three-dimensional resolution of the velocity profile even when only the vertically averaged solution is of interest.

Vertical velocity profiles have been studied numerically in several ways. The work of Blumberg and Mellor[7] is representative of the full finite difference approach. Davies[8] and Heaps and Jones[9] use eigenfunction expansions in the vertical, a distinct and important alternative to that pursued

here. Tee[10] uses either exact vertical solutions for simple viscosity functions or finite differences in the vertical for the more general case, and derives approximate bottom stress parameters for use in a two-dimensional model. This latter work is the closest in spirit to the present paper, which uses finite elements throughout and an exact bottom stress parametrization.

In the present work we solve the three-dimensional linear equations without tampering or further approximating the bottom stress expression. We exploit the established strengths of the finite element method for the horizontal structure, and purposefully use the simplest possible vertical representation: analytic when possible, simple finite elements otherwise. The choice of vertical strategy reflects our desire to simplify as much as possible the pre- and post-processing, which we find to be a significant consumer of analyst and machine time. Additionally, we seek here to pave the way for a fully non-linear three-dimensional time-stepping model based on simple elements. The formulation provides two options, so that either conversion of existing two-dimensional codes or construction of cleaner three-dimensional codes is facilitated.

GOVERNING EQUATIONS

As in Reference 11 we employ the linearized continuity and momentum equations, assuming space–time separation of the form $q(\mathbf{x}, t) = \mathrm{Re}\ [Q(\mathbf{x})e^{j\omega t}]$, with Q the complex amplitude of q:

$$j\omega\zeta + \nabla\cdot(h\bar{\mathbf{V}}) = 0, \tag{1}$$

$$j\omega\mathbf{V} + \mathbf{f}\times\mathbf{V} - \frac{\partial}{\partial z}\left(N\frac{\partial\mathbf{V}}{\partial z}\right) = -g\,\nabla\zeta, \tag{2}$$

in which $\zeta(x, y)$ is the complex amplitude of the free surface elevation, $\mathbf{V}(x, y, z)$ is the complex amplitude of the horizontal velocity, $\bar{\mathbf{V}}(x, y)$ is the vertical average of $\mathbf{V}$, ω is the radian frequency, j is the imaginary unit, $\sqrt{(-1)}$, $h(x, y)$ is the bathymetric depth, $\mathbf{f}$ is the Coriolis vector, directed vertically, $N(x, y, z)$ is the vertical eddy viscosity, g is the acceleration due to gravity, (x, y) are the horizontal co-ordinates, z is the vertical co-ordinate, positive upward, and ∇ is the horizontal operator $(\partial/\partial x, \partial/\partial y)$.

At the surface $(z = 0)$ and bottom $(z = -h)$, boundary conditions are enforced on stress:

$$N\frac{\partial\mathbf{V}}{\partial z} = h\mathbf{\Psi} \quad (z = 0), \tag{3}$$

$$N\frac{\partial\mathbf{V}}{\partial z} = k\mathbf{V} \quad (z = -h), \tag{4}$$

in which $h\mathbf{\Psi}(x, y)$ is the complex amplitude of the atmospheric forcing and k is a linear slip coefficient. Note that the bottom stress is given in terms of the local velocity, not $\bar{\mathbf{V}}$. Vertical averaging of (2) yields

$$j\omega\bar{\mathbf{V}} + \mathbf{f}\times\bar{\mathbf{V}} + \frac{k}{h}\mathbf{V}(-h) = -g\,\nabla\zeta + \mathbf{\Psi}, \tag{5}$$

in which the boundary conditions have been incorporated.

A key feature of these equations is that the bottom stress may be re-expressed in terms of $\bar{\mathbf{V}}$ and $\mathbf{\Psi}$ without introducing any further assumptions or simplifications. This feature was introduced by Lynch and Officer[11] for the case $\mathbf{\Psi} = 0$ and is generalized below. The impact of this is to enable the solution of (1) and (5) as a two-dimensional, horizontal system, either analytically as in the previous paper, or on finite elements as described here. The numerical approach for this two-dimensional problem has been elaborated elsewhere for vertically homogeneous problems[2-6,12] and requires

only minor modifications to fit the present, more general context in which the bottom stress may be out of phase with $\bar{V}$ and/or in a distinctly different direction. The numerical method which emerges for the three-dimensional system thus involves solving the vertical and horizontal portions of the problem separately, in three sequential steps:

(a) Express the bottom stress in terms of $\bar{V}$ and Ψ. This involves solution of simple one-dimensional diffusion equations either analytically, as in Reference 11, or numerically. In the latter case we show below that finite element solutions on common linear elements suffice, involving nothing more than tridiagonal matrix inversions.

(b) Solve the horizontal system, equations (1) and (5), for ζ and the pressure gradient, $g \nabla \zeta$. As mentioned above, established methods using simple linear finite elements may be brought to bear here.

(c) Solve the momentum equation (2) for V, with known pressure gradient. This job is similar to (a) above and in fact the solution for V may be reconstructed from information saved in step (a).

We emphasize that steps (a)–(c) are sequential and need no reiteration. As a result the operation count for the entire three-dimensional problem scales with the two-dimensional calculation, step (b). Specifically, if there are $\mathcal{N}$ nodes in the horizontal grid, with half-bandwidth $\sqrt{\mathcal{N}}$, then the number of operations scales with $\mathcal{N}^2$ for direct, banded LU decomposition.[†] Additional economy in step (b) is available if one uses the 'wave' or Helmholtz equation approach, wherein a second-order differential equation for ζ alone replaces the coupled set (1) and (5) in ζ and $\bar{V}$, with attendant reduction in the limiting matrix decomposition operations by a factor of 3^3.[‡] By taking advantages of these features, we are able to achieve three-dimensional solutions for systems with 1000 nodes in the horizontal in 1–2 minutes of CPU time on a microcomputer with LINPACK rating of 0·16 MFLOPS.[13]

NUMERICAL METHOD

The three-dimensional system is discretized using conventional finite elements in the horizontal plane:

$$\zeta(x, y) = \sum_i \zeta_i \phi_i(x, y), \tag{6}$$

$$V(x, y, z) = \sum_i V_i(Z)\phi_i(x, y), \tag{7}$$

in which ϕ_i are the horizontal finite element bases, and $Z = z/h$ is the normalized depth (see Figure 1). We will use both continuum and finite element representation of the $V_i(Z)$. In either case we employ a Galerkin method in the horizontal, with the inner product notation $\langle \cdot, \cdot \rangle$ indicating a quadrature approximation to $\int \int (\cdot, \cdot) \, dx \, dy$. As in previous papers (e.g. Reference 14) we employ 'integral lumping', in which the quadrature points coincide with the nodes. This results in the diagonalization of the mass matrix, an enormous advantage in dealing with the momentum equation.

[†] The LU decomposition of a matrix obtained a mesh with $\mathcal{N}$ nodes with 1 degree of freedom per node and bandwidth $\sqrt{\mathcal{N}}$ will require $\mathcal{N} \times \sqrt{\mathcal{N}} \times \sqrt{\mathcal{N}} = \mathcal{N}^2$ operations.

[‡] A formulation resulting in 3 degrees of freedom per node would yield a matrix with $3\mathcal{N}$ equations and of bandwidth of order $3\sqrt{\mathcal{N}}$. Thus the number of operations for the LU decomposition would be $3\mathcal{N} \times 3\sqrt{\mathcal{N}} \times 3\sqrt{\mathcal{N}} = 3^3\mathcal{N}^2$.

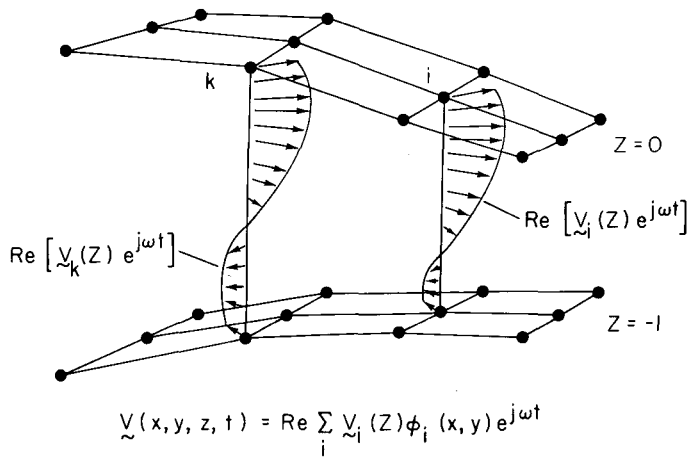$$V(x, y, z, t) = \mathrm{Re} \sum_i V_i(Z)\phi_i(x, y)e^{j\omega t}$$

Figure 1. Discretization of velocity on horizontal finite element grid with the complex functions $V_i(Z)$ defined beneath each node. $Z \equiv z/h$

Vertical structure and bottom stress

To begin with, we investigate the solution of the momentum equations (2)–(4) as a response to gravity and wind forcing. Of course the gravity force is at the outset unknown; the key is to extract the bottom stress parameters in spite of this fact. To enhance this exposition, we define the gravity force as

$$\mathbf{G} \equiv -g\nabla\zeta. \tag{8}$$

(i) *Non-rotating systems*. Fundamental to the solution of (2) is a simpler, scalar diffusion equation:

$$j\omega\mu - \frac{\mathrm{d}}{\mathrm{d}Z}\left(\frac{N}{h^2}\frac{\mathrm{d}\mu}{\mathrm{d}Z}\right) = G, \tag{9}$$

with boundary conditions:

$$\frac{N}{h}\frac{\mathrm{d}\mu}{\mathrm{d}Z} = h\psi \quad (Z = 0), \tag{10}$$

$$\frac{N}{h}\frac{\mathrm{d}\mu}{\mathrm{d}Z} = k\mu \quad (Z = -1). \tag{11}$$

In the absence of rotation, both V_x and V_y satisfy (9)–(11) with appropriate values of G and ψ. As in Reference 11 we express the solution to (9) as the sum of homogeneous solutions μ_1, μ_2 plus the particular solution $G/(j\omega)$:

$$\mu = \frac{G}{j\omega} + c_1\mu_1(Z) + c_2\mu_2(Z). \tag{12}$$

Application of the boundary conditions determines the constants c_1 and c_2. The result is

$$\mu(Z) = \frac{G}{j\omega}\left[1 - \frac{A(Z)}{B}\right] + \psi\left[\frac{h^2}{N(0)}\frac{E(Z)}{B}\right], \tag{13}$$

with

$$A = \det\begin{vmatrix} \dot{\mu}_1(0) & \dot{\mu}_2(0) \\ \mu_1(Z) & \mu_2(Z) \end{vmatrix}, \tag{14}$$

$$B = \det \begin{vmatrix} \dot{\mu}_1(0) & \dot{\mu}_2(0) \\ [\mu_1 - N\dot{\mu}_1/(kh)]|_{-1} & [\mu_2 - N\dot{\mu}_2/(kh)]|_{-1} \end{vmatrix}, \tag{15}$$

and

$$E = \det \begin{vmatrix} \mu_1(Z) & \mu_2(Z) \\ [\mu_1 - N\dot{\mu}_1/(kh)]|_{-1} & [\mu_2 - N\dot{\mu}_2/(kh)]|_{-1} \end{vmatrix}, \tag{16}$$

where the overdot indicates d/dZ. Equation (13) may also be arrived at by inspection of the linear system (9)–(11) in the intuitively appealing form

$$\mu(Z) = GP_1(Z) + \psi P_2(Z), \tag{17a}$$

with

$$P_1(Z) = \frac{1}{j\omega}\left[1 - \frac{A(Z)}{B}\right], \quad P_2(Z) = \left[\frac{h^2}{N(0)}\frac{E(Z)}{B}\right], \tag{17b}$$

in which $P_1(Z)$ is the solution to equations (9)–(11) with $G = 1, \psi = 0$, and $P_2(Z)$ is obtained with $G = 0, \psi = 1$. Form (13) is useful when dealing with closed-form solutions, whereas form (17a) is much more appealing when solving (9)–(11) numerically.

The unknown G in (17a) may be replaced with $\bar{\mu}$ (the vertical average of μ) by first taking the average of (17a) and rearranging:

$$G = \frac{\bar{\mu} - \psi\bar{P}_2}{\bar{P}_1}. \tag{18}$$

Elimination of G in (17a) then yields

$$\mu(Z) = \left(\frac{P_1(Z)}{\bar{P}_1}\right)\bar{\mu} + \left(P_2(Z) - P_1(Z)\frac{\bar{P}_2}{\bar{P}_1}\right)\psi, \tag{19}$$

and the bottom stress is then given by

$$k\mu(-1) = \left(\frac{kP_1(-1)}{\bar{P}_1}\right)\bar{\mu} - \left(\frac{kP_1(-1)}{\bar{P}_1}\bar{P}_2 - kP_2(-1)\right)\psi. \tag{20}$$

Note that this is the desired form—bottom stress in terms of $\bar{\mu}$ and ψ, independent of the value of the gravity term G. To facilitate the linkage to the two-dimensional problem we define bottom stress parameters τ and α:

$$\tau \equiv \frac{kP_1(-1)}{h\bar{P}_1}, \tag{21}$$

$$\alpha = \tau\bar{P}_2 - \frac{k}{h}P_2(-1), \tag{22}$$

so that the final result is

$$k\mu(-1) = \tau h\bar{\mu} - \alpha\psi h. \tag{23}$$

Note that τ and α are dependent upon $\omega, N(Z), h$ and k, and thus vary with frequency as well as (x, y) location.

Equivalent expressions for τ and α may be obtained in terms of the homogeneous solutions μ_1 and μ_2:

$$\tau = \frac{k}{h}\left[\frac{B - A(-1)}{B - \bar{A}}\right], \tag{24}$$

$$\alpha = \frac{h}{N(0)}\left[\frac{\tau h \bar{E} - kE(-1)}{B}\right]. \tag{25}$$

In the Appendix we record some useful identities which lead to alternative expressions for τ and α.

(ii) *Rotating systems.* When rotation is present in the system, we define two linear combinations of V_x and V_y:

$$v^+ = \frac{V_x + jV_y}{2}, \quad v^- = \frac{V_x - jV_y}{2}, \tag{26}$$

and the inverse relations

$$V_x = v^+ + v^-; \quad jV_y = v^+ - v^-. \tag{27}$$

Equations (9)–(11) govern $v^\pm$ with the frequency shifted to $\omega \pm f$:

$$j(\omega \pm f)v^\pm - \frac{d}{dZ}\left(\frac{N}{h^2}\frac{dv^\pm}{dZ}\right) = G^\pm, \tag{28}$$

$$\frac{N}{h}\frac{dv^\pm}{dZ} = h\psi^\pm \quad (Z = 0), \tag{29}$$

$$\frac{N}{h}\frac{dv^\pm}{dZ} = kv^\pm \quad (Z = -1), \tag{30}$$

where the forcing terms are

$$G^\pm = \frac{G_x \pm jG_y}{2}, \tag{31}$$

$$\psi^\pm = \frac{\psi_x \pm j\psi_y}{2}. \tag{32}$$

From the derivation above, we thus have two values of τ and α, one each for v^+ and v^-:

$$kv^\pm(-1) = \tau^\pm h\bar{v}^\pm - \alpha^\pm \psi^\pm h. \tag{33}$$

The bottom stress $k\mathbf{V}(-1)$ may be reconstructed using (27) and (33):

$$k\mathbf{V}(-1) = \left(\frac{\tau^+ + \tau^-}{2}\right)h\bar{\mathbf{V}} - j\left(\frac{\tau^+ - \tau^-}{2}\right)\hat{\mathbf{z}} \times h\bar{\mathbf{V}}$$
$$- \left(\frac{\alpha^+ + \alpha^-}{2}\right)h\mathbf{\Psi} + j\left(\frac{\alpha^+ - \alpha^-}{2}\right)\hat{\mathbf{z}} \times h\mathbf{\Psi}, \tag{34}$$

where $\hat{\mathbf{z}}$ is the unit vector along the z axis. Finally, use of (34) in the vertically averaged momentum equation yields

$$j\omega\bar{\mathbf{V}} + \mathbf{f}' \times \bar{\mathbf{V}} + \tau'\bar{\mathbf{V}} = -g\nabla\zeta + \mathbf{\Psi}', \tag{35}$$

where the quantities $\mathbf{f}'$, τ' and $\mathbf{\Psi}'$ all contain contributions from the bottom stress:

$$\mathbf{f}' = \mathbf{f} - j\left(\frac{\tau^+ - \tau^-}{2}\right)\hat{\mathbf{z}}, \tag{36}$$

$$\tau' = \frac{\tau^+ + \tau^-}{2}, \tag{37}$$

$$\Psi' = \Psi\left[1 + \left(\frac{\alpha^+ + \alpha^-}{2}\right)\right] - j\left(\frac{\alpha^+ - \alpha^-}{2}\right)\hat{z} \times \Psi. \tag{38}$$

Equation (35) has the form of the conventional two-dimensional momentum equation; however all of the vertical detail is embodied without loss of information in the parameters f', τ' and Ψ'. These 'virtual' parameters are shifted in magnitude, phase and (in the case of Ψ') direction from their physical three-dimensional analogues which are customarily used without modification in two-dimensional analyses. From (35) we may in turn express $\bar{V}$ in the conventional two-dimensional form:

$$\bar{V} = -\left(\frac{(j\omega + \tau')(g\nabla\zeta - \Psi') - f' \times (g\nabla\zeta - \Psi')}{(j\omega + \tau')^2 + f'^2}\right). \tag{39}$$

Equations (35) and/or (39) provide a simple recipe for upgrading any conventional program which solves the two-dimensional harmonic equations—one need only compute and use the virtual parameters f', τ' and Ψ' in place of their physical values. Additionally, the above analysis provides a framework for studying bottom stress, for example as in Reference 11 for the special case of constant N.

The equivalent of (39) may however be obtained more simply by avoiding the intermediate step of computing the bottom stress. With

$$v^{\pm}(Z) = G^{\pm}P_1^{\pm}(Z) + \psi^{\pm}P_2^{\pm}(Z) \tag{40}$$

we may reconstruct V_x, V_y according to (27). The result,

$$V(Z) = G\left(\frac{P_1^+ + P_1^-}{2}\right) - j\left(\frac{P_1^+ - P_1^-}{2}\right)\hat{z} \times G + \Psi\left(\frac{P_2^+ + P_2^-}{2}\right) - j\left(\frac{P_2^+ - P_2^-}{2}\right)\hat{z} \times \Psi, \tag{41}$$

is computationally more appealing but intuitively less informative. (Recall that $G \equiv -g\nabla\zeta$.) The vertical average of (41) is straightforward. Equation (41) may of course be expressed in terms of $\mu_{1,2}^{\pm}$ via equation (17b).

The quantities f', τ', Ψ', or equivalently $\bar{P}_{1,2}^{\pm}$, are ultimately needed for the horizontal solution at all nodes in the horizontal mesh. In some simple cases analytical expressions are available (a partial summary can be found in Reference 11). More generally we obtain Galerkin finite element solutions to equation (9) on simple one-dimensional linear elements. In this case four tridiagonal solutions are required under each node: either $\mu_{1,2}^{\pm}$ or $P_{1,2}^{\pm}$. These then generate the required parameters in equations (39) and (41). The four tridiagonal solutions are saved for reconstruction of $V(Z)$ after ζ has been obtained (see the section on vertical structure below).

Horizontal structure: computation of ζ

Equations (1) and either (35), (39) or (41) constitute a conventional shallow-water problem in ζ and $\bar{V}$. Based on prior experience[4,5,14] we avoid the primitive equation approach in which (1) and (35) are solved simultaneously. Instead we use a 'wave' or Helmholtz equation, i.e. a second-order equation in ζ obtained by eliminating $\bar{V}$ from (1). Using (1) and (39)

$$j\omega\zeta - \nabla\cdot\left[\frac{(j\omega + \tau')(gh\nabla\zeta - h\Psi') - f' \times (gh\nabla\zeta - h\Psi')}{(j\omega + \tau')^2 + f'^2}\right] = 0, \tag{42}$$

or equivalently, using the average of (41),

$$j\omega\zeta - \nabla\cdot\left[\left(\frac{\bar{P}_1^+ + \bar{P}_1^-}{2}\right)gh\,\nabla\zeta - j\left(\frac{\bar{P}_1^+ - \bar{P}_1^-}{2}\right)\hat{z}\times gh\,\nabla\zeta - \left(\frac{\bar{P}_2^+ + \bar{P}_2^-}{2}\right)h\mathbf{\Psi}\right.$$

$$\left. + j\left(\frac{\bar{P}_2^+ - \bar{P}_2^-}{2}\right)\hat{z}\times h\mathbf{\Psi}\right] = 0.\tag{43}$$

From (42) and (43) we obtain the Galerkin forms

$$\langle j\omega\zeta, \phi_i\rangle + \left\langle\left[\frac{(j\omega+\tau')gh\,\nabla\zeta - \mathbf{f}'\times gh\nabla\zeta}{(j\omega+\tau')^2 + f'^2}\right]\cdot\nabla\phi_i\right\rangle$$

$$= -\oint h\bar{\mathbf{V}}\cdot\hat{\mathbf{n}}\phi_i\,\mathrm{d}s + \left\langle\left[\frac{(j\omega+\tau')h\mathbf{\Psi}' - \mathbf{f}'\times h\mathbf{\Psi}'}{(j\omega+\tau')^2 + f'^2}\right]\cdot\nabla\phi_i\right\rangle\tag{44}$$

and

$$\langle j\omega\zeta, \phi_i\rangle + \left\langle\left[\left(\frac{\bar{P}_1^+ + \bar{P}_1^-}{2}\right)gh\,\nabla\zeta - j\left(\frac{\bar{P}_1^+ - \bar{P}_1^-}{2}\right)\hat{z}\times gh\,\nabla\zeta\right]\cdot\nabla\phi_i\right\rangle$$

$$= -\oint h\bar{\mathbf{V}}\cdot\hat{\mathbf{n}}\phi_i\,\mathrm{d}s + \left\langle\left[\left(\frac{\bar{P}_2^+ + \bar{P}_2^-}{2}\right)h\mathbf{\Psi} + j\left(\frac{\bar{P}_2^+ - \bar{P}_2^-}{2}\right)\hat{z}\times h\mathbf{\Psi}\right]\cdot\nabla\phi_i\right\rangle.\tag{45}$$

We express ζ in the finite element basis ϕ, equation (6), and solve on simple C^0 elements. All domain and boundary integrals are evaluated numerically, with quadrature points at the nodes. Boundary conditions on $\bar{\mathbf{V}}\cdot\hat{\mathbf{n}}$ are enforced as natural conditions via the surface integrals. Boundary conditions on ζ are satisfied exactly, and the associated Galerkin equations are used to compute $\bar{\mathbf{V}}\cdot\hat{\mathbf{n}}$ via the surface integral. This procedure conserves mass exactly in the numerical solution.[6]

Vertical structure: computation of $\mathbf{V}$

Once ζ is known, we reconstruct $\mathbf{V}(Z)$ under each node from the saved $P(Z)$ or $\mu(Z)$. A Galerkin form of (41) is employed, together with the discretizations (6) and (7). The result using integral lumping is especially simple:

$$\mathbf{V}_i(Z) = \left(\frac{P_1^+ + P_1^-}{2}\right)_i\mathbf{G}_i - j\left(\frac{P_1^+ - P_1^-}{2}\right)_i\hat{z}\times\mathbf{G}_i + \left(\frac{P_2^+ + P_2^-}{2}\right)_i\mathbf{\Psi}_i - j\left(\frac{P_2^+ - P_2^-}{2}\right)_i\hat{z}\times\mathbf{\Psi}_i,\tag{46}$$

with nodal gravity forcing defined as

$$\mathbf{G}_i \equiv \frac{\langle -g\,\nabla\zeta, \phi_i\rangle}{\langle\phi_i, \phi_i\rangle}\tag{47}$$

(recall that $\langle\cdot,\cdot\rangle$ indicates integration over (x, y) via nodal quadrature). In effect, a simple post-processing of the ζ solution returns $\mathbf{V}_i(Z)$, with no further matrix manipulations.

When $\mathbf{V}\cdot\hat{\mathbf{n}}$ is prescribed on a boundary, we satisfy this condition exactly, in the following manner. First, a nodal normal $\hat{\mathbf{n}}_i$ is defined.[15] In our case we retain the simple definition

$$\hat{\mathbf{n}}_i \equiv \frac{\oint\hat{\mathbf{n}}\phi_i\,\mathrm{d}s}{\oint\phi_i\,\mathrm{d}s}\tag{48}$$

from previous studies (e.g. Reference 14). We then retain the local tangential component of (46) and sacrifice the normal component in favour of the boundary condition.

When only $\bar{\mathbf{V}} \cdot \hat{\mathbf{n}}$ is known, e.g. at a boundary where ζ is specified, we use this information to compute $\mathbf{G} \cdot \hat{\mathbf{n}}$. From the vertical average of (46) we have

$$
(\mathbf{G} \cdot \hat{\mathbf{n}})_i = \frac{\left\{ \bar{\mathbf{V}} \cdot \hat{\mathbf{n}} - j\left(\dfrac{\bar{P}_1^+ - \bar{P}_1^-}{2}\right)\mathbf{G} \cdot \hat{\mathbf{t}} - \left(\dfrac{\bar{P}_2^+ + \bar{P}_2^-}{2}\right)\mathbf{\Psi} \cdot \hat{\mathbf{n}} - j\left(\dfrac{\bar{P}_2^+ - \bar{P}_2^-}{2}\right)\mathbf{\Psi} \cdot \hat{\mathbf{t}} \right\}_i}{\left(\dfrac{\bar{P}_1^+ + \bar{P}_1^-}{2}\right)_i}, \tag{49}
$$

where (n, t) are a local right-handed co-ordinate system. We retain the tangential component of $\mathbf{G}$ as computed by equation (47) and sacrifice the normal component in favour of (49), which enforces the normal constraint on $\bar{\mathbf{V}}$.

TEST CASES: ANALYTICAL VERTICAL STRUCTURE

For a first series we used the simplest vertical structure, $\partial N / \partial Z = 0$, and the exact analytic solutions for the vertical from Reference 11. The sequence of computations is summarized as follows:

(a) Compute $\tau^\pm, \alpha^\pm$ for each horizontal node using equations (24) and (25).
(b) Compute $\tau', \mathbf{f}'$ and $\mathbf{\Psi}'$ for each node via (36)–(38).
(c) Solve (44) for ζ.
(d) Reconstruct $\mathbf{V}_i(Z)$ beneath each node via (46) subject to the boundary conditions.

In this series the exact homogeneous solutions are

$$
\mu_{1,2} = \exp\left(\pm Z \sqrt{\left(\frac{j\omega h^2}{N}\right)} \right) \tag{50}
$$

and the relations between μ and P are given by equations (14)–(17). As a base of comparison we use the solutions of Lynch and Gray.[16] Because these require constant values of τ' and $\mathbf{\Psi}'$, N and k must vary with (x, y) such that $N/(\omega h^2)$ and kh/N are constant.
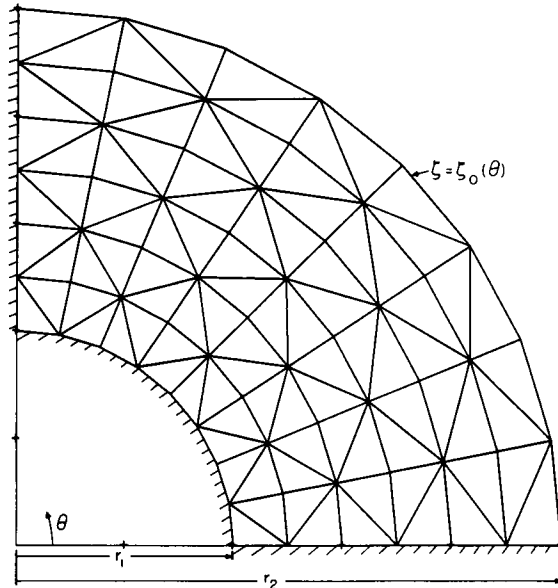
Figure 2. Geometry of test cases and coarse grid consisting of 63 nodes and 96 elements. The specified tidal amplitude is ζ_0; values for r_1, r_2 and the bathymetry are given in the text. The solid no-flux boundary is indicated by the hatched lines

The first test was one introduced by Gray and Lynch[17] and is illustrated in Figure 2. The bathymetry is given by $h = h_0 r^2$, and a constant tidal amplitude ζ_0 is prescribed on the open boundary. Parameters are

$$r_1 = 60{,}960 \, \text{m},$$

$$r_2 = 152{,}400 \, \text{m},$$

$$h_0 = 3 \cdot 048 r_1^2 \, \text{m}^{-1},$$

$$\zeta_0 = 1 \cdot 0 \, \text{m},$$

$$\omega = 1 \cdot 41 \times 10^{-4} \text{s}^{-1},$$

$$kh/N = \infty \, (\text{no slip}),$$

$$\omega h^2/N = 10,$$

$$\mathbf{f} = 0.$$

In Figure 3 we show plots of $|\zeta|$ against τ along two different radial lines, compared with the analytic solution. The accuracy is comparable to the analogous two-dimensional results obtained previously.
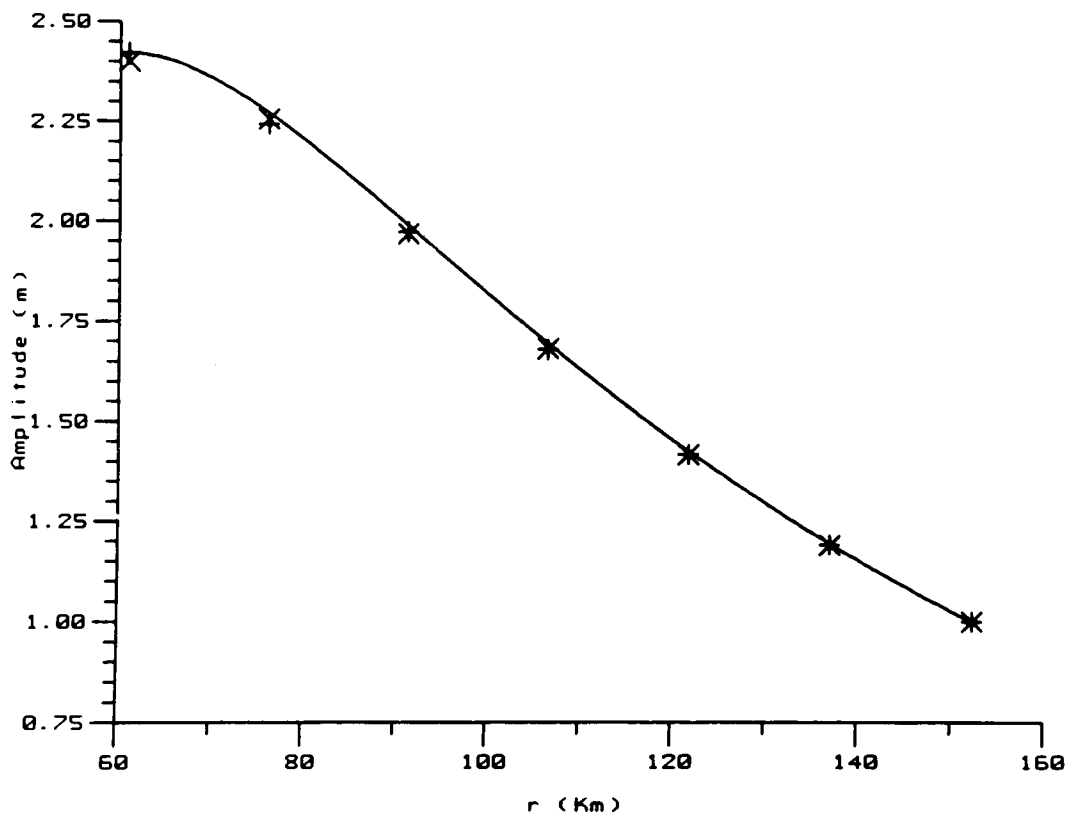
Figure 3. Comparison of the analytic (solid line) and numerical elevation amplitude as a function of r. Numerical solutions computed on the coarse mesh (Figure 2) at $\theta = 0$ (indicated by the '$\times$') and at $\theta = \Delta\theta_c$ (indicated by the '$+$'). The prescribed tidal amplitude ζ_0 is constant on the open boundary

A more interesting test is obtained on this grid by varying ζ_0 along the open boundary. In Figures 4(a), (b) we show contours of $|\zeta|$ obtained with $\zeta_0 = \cos(2\theta)$ such that high water occurs for $\theta < 45°$ when low water is occurring for $\theta > 45°$. Results are reasonable, although the grid is too coarse—only 16 elements per wavelength in the θ direction. Figure 4(c) shows results obtained by doubling the resolution—the finer grid appears in Figure 5. Sample plots of $|\zeta|$ against r are given in Figures 4(d) and (e) for the two grids and provide a better quantification of the error. The maximum error occurs at $r = r_1$ where only the natural boundary conditions are imposed on ζ, whereas the error vanishes at $r = r_2$ where Dirichlet conditions are imposed. Vector plots of $\mathbf{V}$ are given for the fine grid in Figure 6 (numerical) and Figure 7 (analytic), at three different vertical levels. The agreement is quite satisfactory. In Figure 8 we show V_x and V_y against Z at a single point in the mesh, at several points in the tidal cycle. Again the agreement is very satisfying. Generally the velocities show a phase lead at the bottom relative to the top, as pointed out by Lynch and Officer.[11] This is manifest in the veering with depth as shown in Figure 9.

A third test case involves the same geometry with a steady, uniform wind directed everywhere parallel to $\theta = 45°$. As in Reference 14, the special boundary condition

$$\zeta_0 = \frac{h|\mathbf{\Psi}'|r^2}{gh}\cos(\theta - 45°) \tag{51}$$

results in $\bar{\mathbf{V}} = \mathbf{0}$ everywhere (analytically) when the bathymetry is constant and $\mathbf{f} = \mathbf{0}$. We solved this problem on the fine grid with h increased to 50m everywhere, and obtained essentially perfect results. A plot of ζ appears in Figure 10 and agrees with the analytic solution to five significant figures. Computed values of $\bar{\mathbf{V}}$ were of the order of 10^{-5} m/s; by contrast, velocities at the surface were of the order of 0.5 m/s. Plots of $\mathbf{V}$ at different levels appear in Figure 11. Since $\nabla\zeta$ is essentially exact and there is no vertical discretization error, the computed $\mathbf{V}(Z)$ is exact also. Figure 12 shows the $\mathbf{V}(Z)$ at a selected mesh point.

Finally, we added rotation equal to a latitude of $45°$N and closed the boundary at $r = r_2 (\bar{\mathbf{V}} \cdot \hat{\mathbf{n}} = 0)$. (At $\theta = 45°$ we enforced $\zeta = 0$ to remove the arbitrary constant from the solution.) As in the previous case, the analytic solution has $g\nabla\zeta = \mathbf{\Psi}' = $ constant and thus $\bar{\mathbf{V}} = \mathbf{0}$ everywhere. As above, our numerical $\bar{\mathbf{V}}$ was of the order of 10^{-5} m/s. Figure 13 shows the expected slight rotation of $\nabla\zeta$ relative to the above case (see equation (38) with $\mathbf{f} \neq 0$). Plots of $\mathbf{V}$ appear in Figures 14 and 15, with the surface currents at roughly $45°$ from the wind direction. The veering with depth is also illustrated in Figure 16.

VERTICAL DISCRETIZATION ERROR

The results above demonstrate the capabilities of a finished three-dimensional model. The major limitation of this model is our inability to solve the periodic diffusion equation (9) with variable $N(Z)$. To overcome this we solve (9) numerically, for arbitrary $N(Z)$, thereby adding much more generality at the expense of an additional discretization error. The horizontal discretization error present in the above solutions has been studied extensively.[18-23] Thus we present here a brief study of the vertical discretization error alone, with the objective of defining some rules of thumb for establishing the vertical grid spacing ΔZ. (In practice of course, the horizontal discretization also affects the error in the vertical.)

As above, we take the simplest case, $\partial N/\partial Z = 0$, and solve (9) on equal-length linear elements with integral lumping. Our measure of error is based on the bottom stress parameter τ:

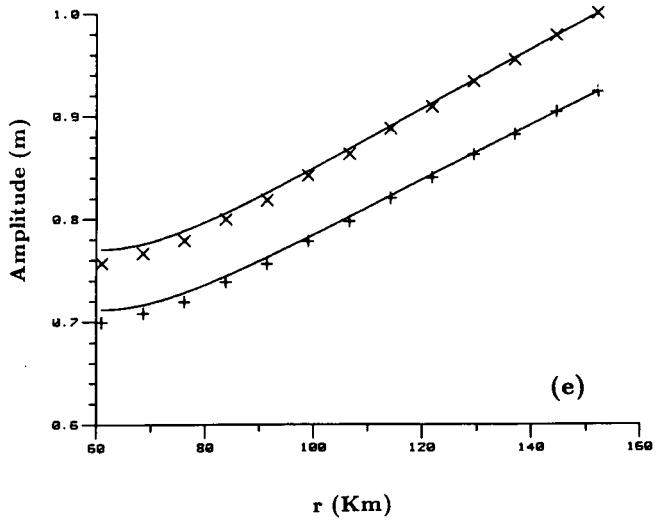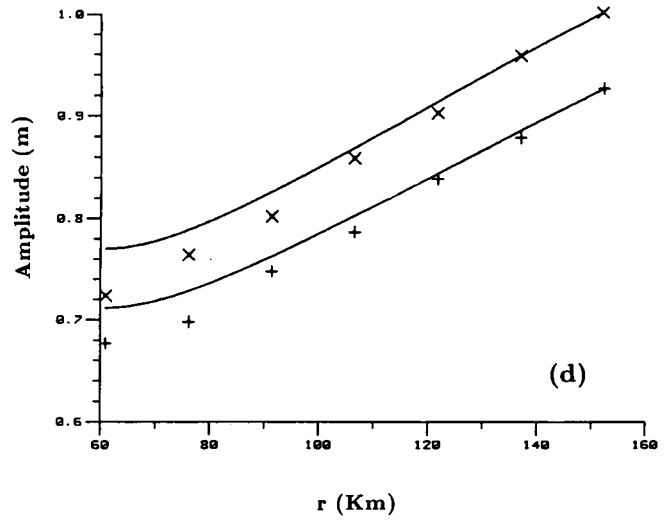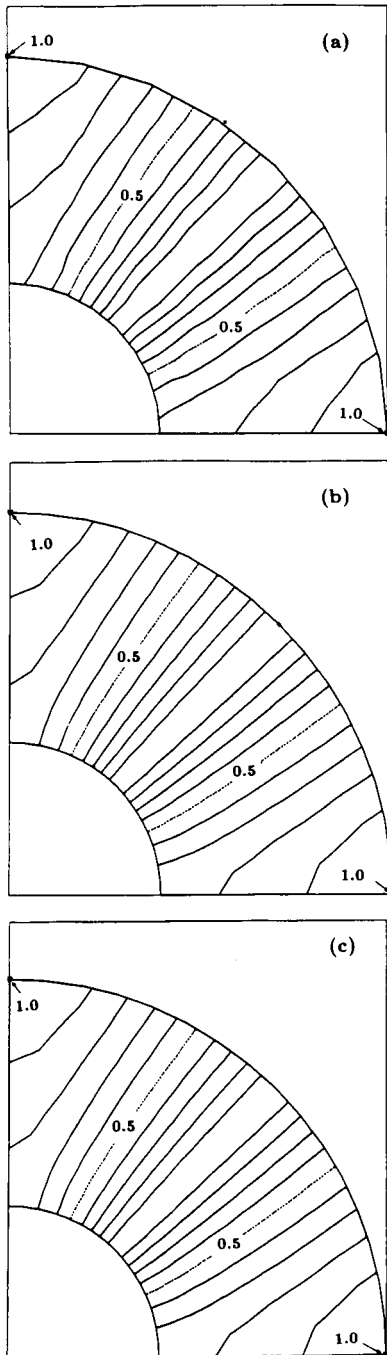$$\varepsilon = \left|\frac{\tau_n - \tau_a}{\tau_a}\right|. \tag{52}$$

Figure 4. Tidal amplitudes in 0·1 m intervals for prescribed tidal amplitude $\zeta_0 = \cos(2\theta)$ at $r = r_2$. (a) Numerical result with the coarse mesh; (b) analytic result interpolated on the fine mesh (Figure 5); (c) numerical result with the fine mesh; (d) comparison of analytic tidal amplitude (solid lines) with numerical solutions as a function of r for $\theta = 0$ (indicated by the '+') and for $\theta = \Delta\theta$ (indicated by the '×') on the coarse mesh; (e) comparison of analytic tidal amplitude (solid lines) with numerical solutions as a function of r for $\theta = 0$ (indicated by the '+') and for $\theta = 2\Delta\theta_r$ (indicated by the '×') on the refined mesh. Note that θ-spacing on the refined mesh ($\Delta\theta_r$) is half that of the coarse mesh ($\Delta\theta_c$)
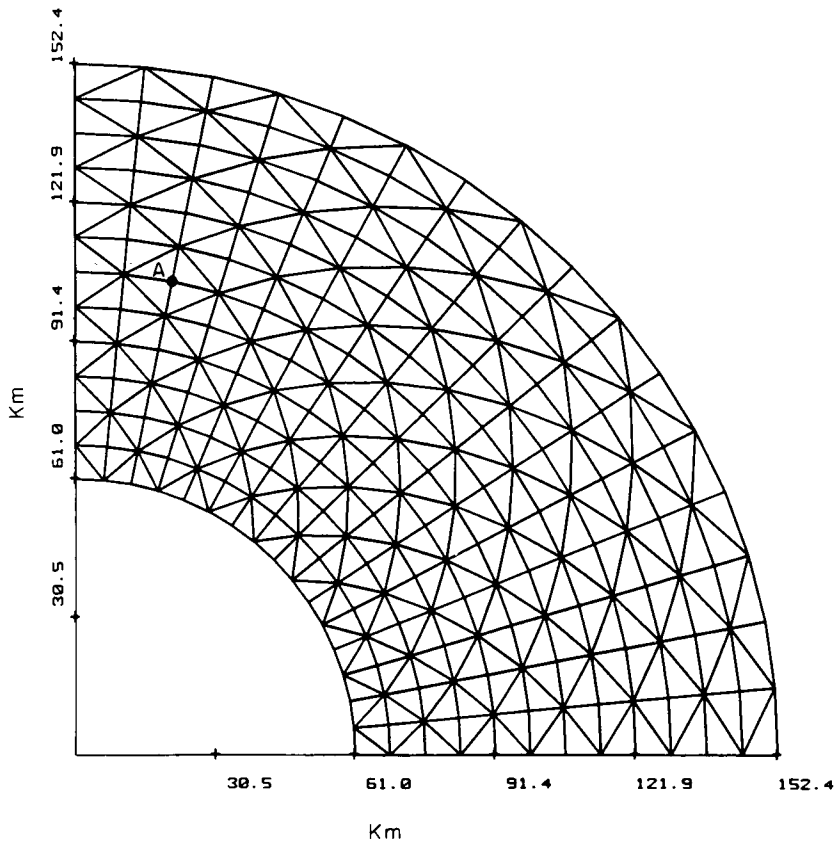
Figure 5. Refined mesh with 221 nodes and 384 elements. The node labeled 'A' is used for sampling velocity profiles discussed in later sections

Herein τ_n is simply computed from the numerical solution according to (21), whereas τ_a is evaluated exactly, as in Reference 11, equation (33). There are three dimensionless parameters:

$$W \equiv \frac{\omega h^2}{N},$$ (53a)

$$K \equiv \frac{kh}{N},$$ (53b)

$$n \equiv \frac{\delta}{\Delta z},$$ (53c)

in which δ is the 'skin depth' or e-folding depth for periodic diffusion:

$$\delta \equiv \sqrt{\left(\frac{2N}{\omega}\right)}.$$ (54)

With these definitions the actual number of elements used is

$$m \equiv \frac{h}{\Delta z} = n \sqrt{\left(\frac{W}{2}\right)},$$ (55)
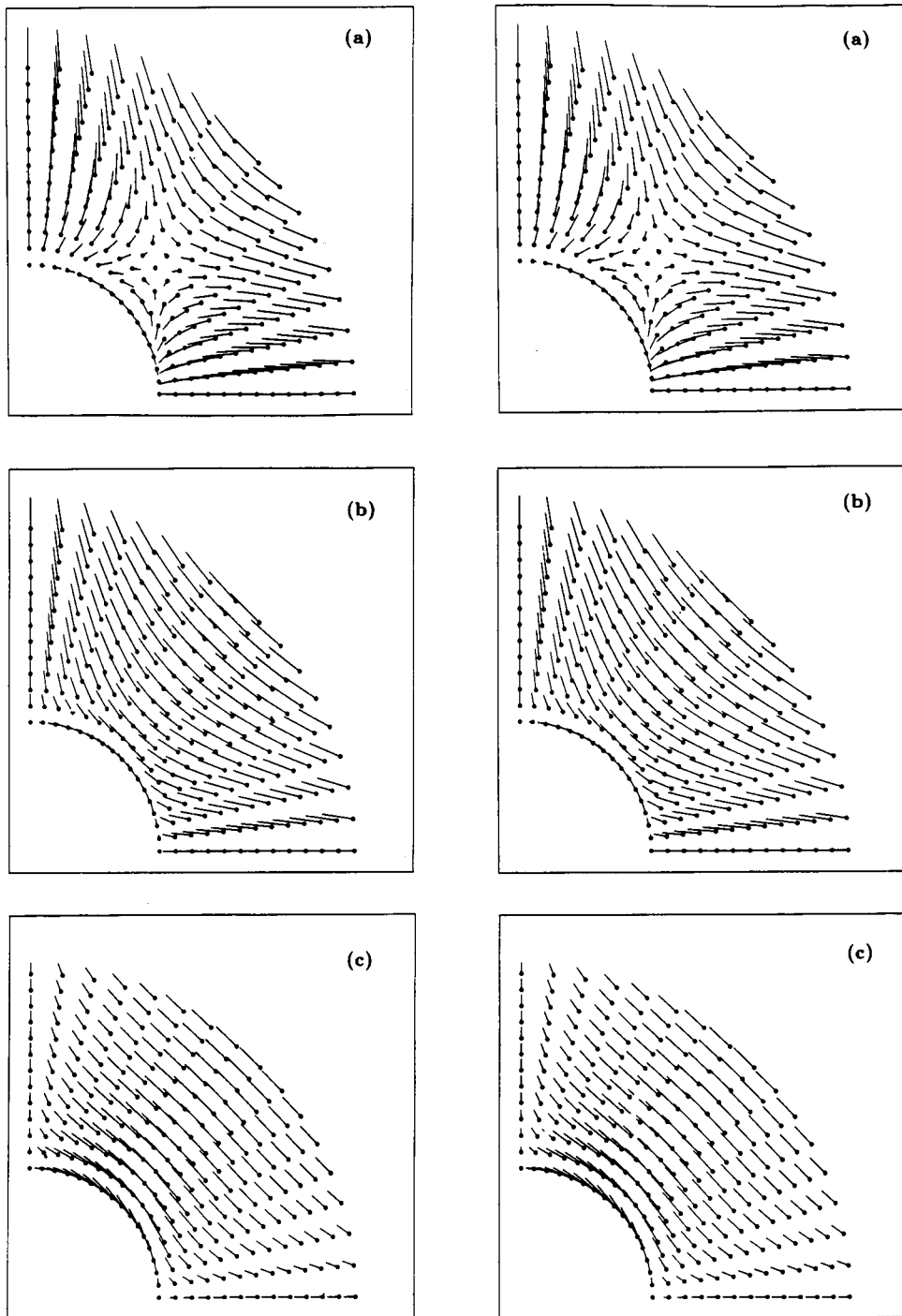
Figure 6. Numerical velocities at $t = 0$ forced by $\zeta_0 = \cos(2\theta)$ at the surface (a), at mid-depth $Z = 0.4$(b) and one level above the bottom (c). The maximum velocity is 0.1814 m/s in (a), 0.2328 m/s in (b) and 0.2223 m/s in (c)

Figure 7. Analytic counterpart of Figure 6. The maximum velocity is 0.1824 m/s in (a), 0.2336 m/s in (b) and 0.2256 m/s in (c)
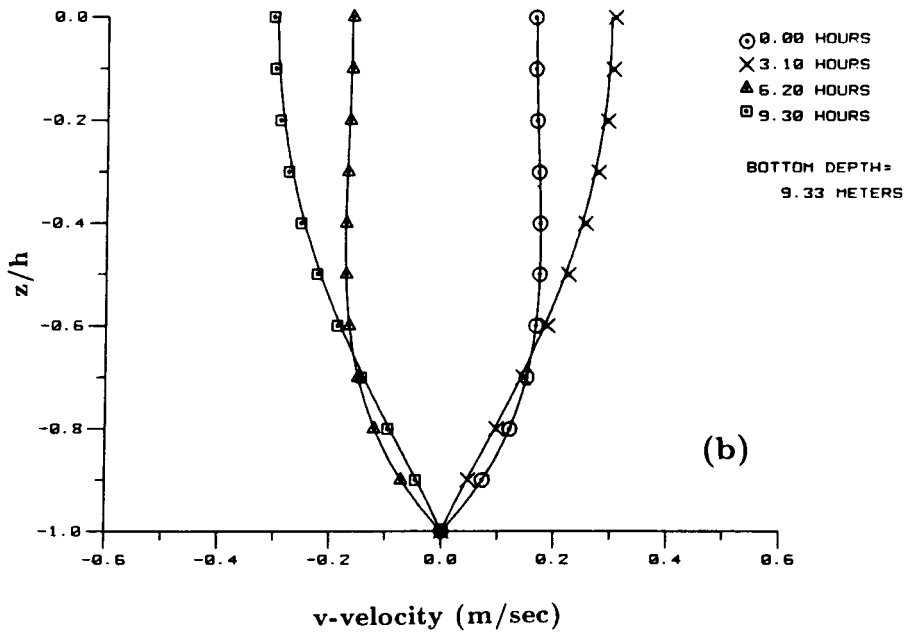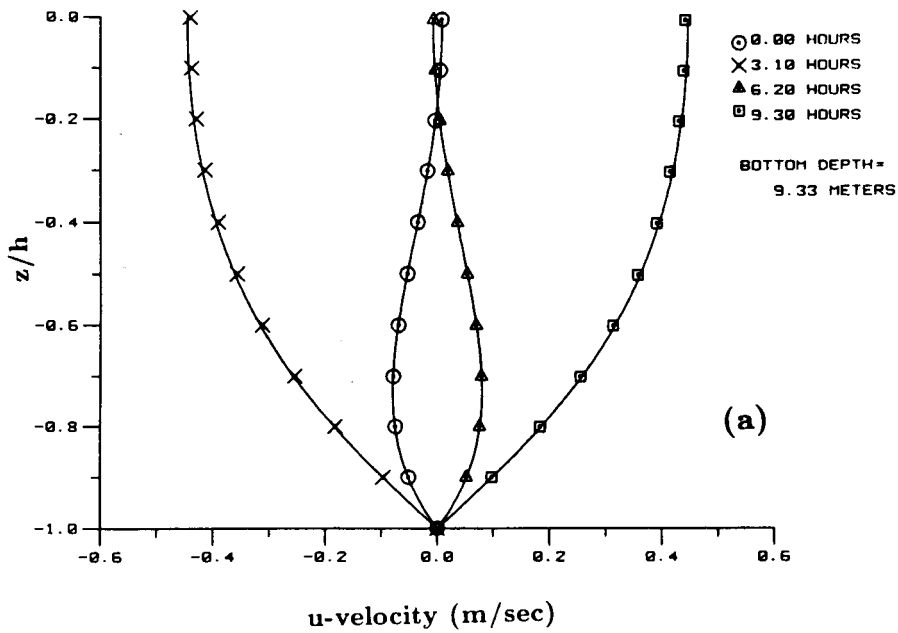
Figure 8. Comparison of exact (solid lines) and numerical velocity profiles at four times in the tidal cycle at mesh-point A (see Figure 5):(a) *u*-component; (b) *v*-component
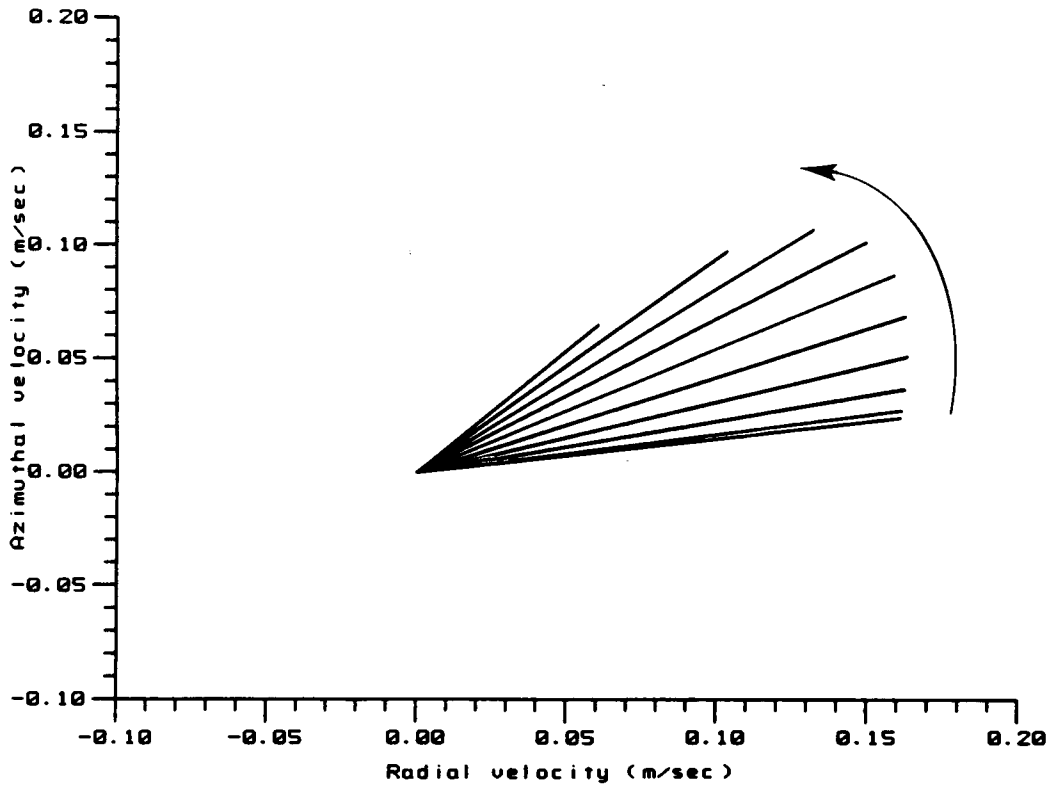
Figure 9. Hodograph of velocity at point A at $t = 0$. The arrow indicates the direction of the current veering with depth, from surface to bottom. Note that the maximum velocity in this instance does not occur at the surface (refer to Figure 8)
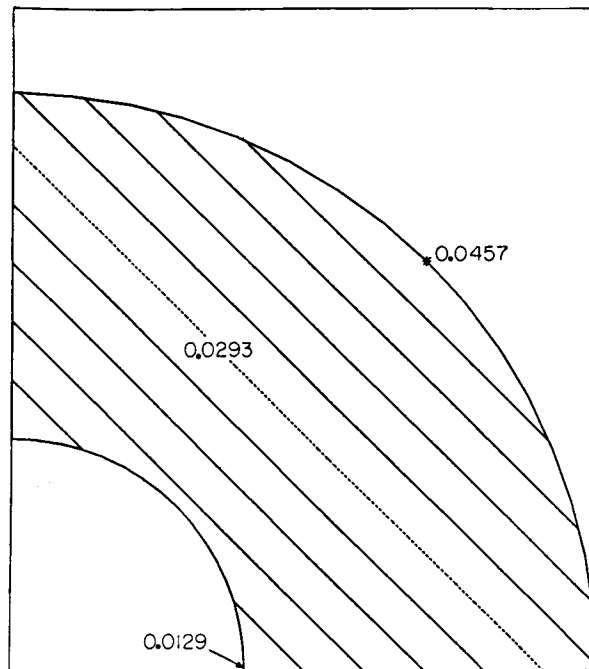
Figure 10. Elevation response (in metres) to steady wind forcing in the $\theta = 45°$ direction without rotation
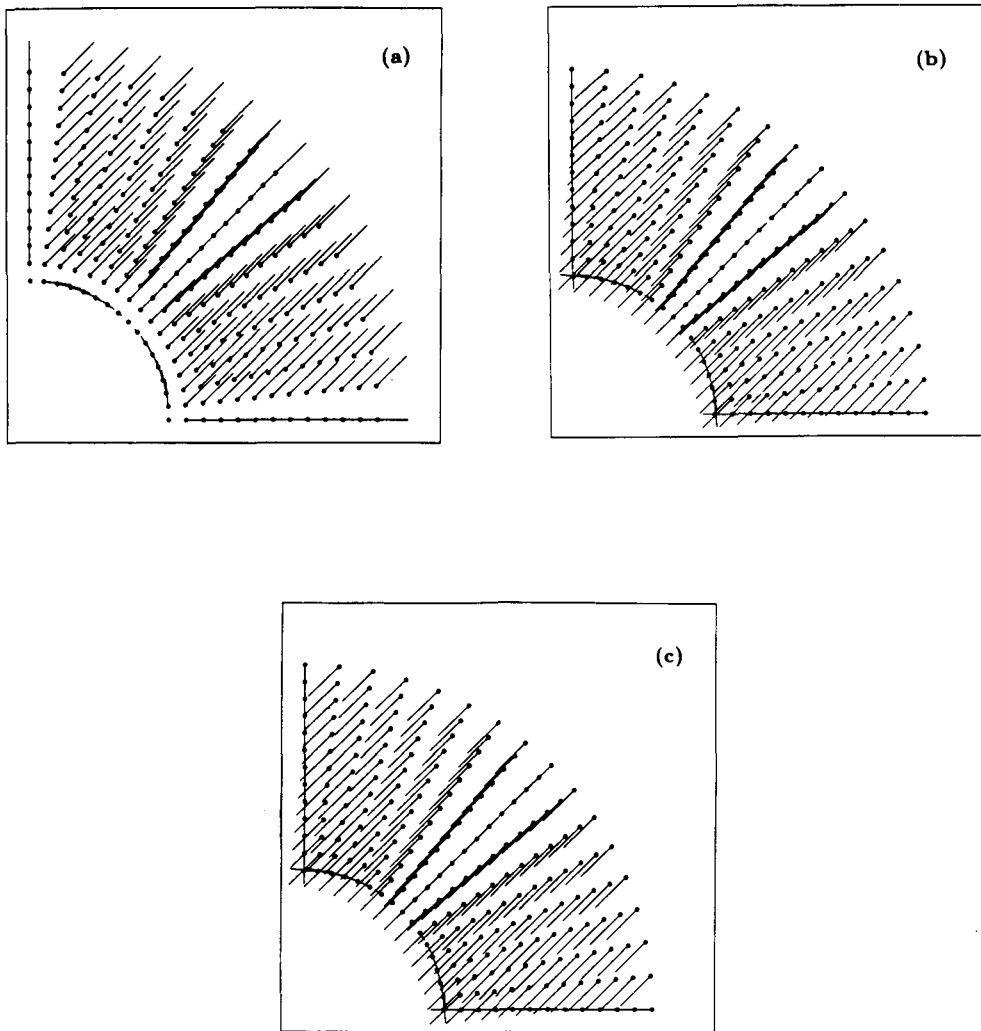
Figure 11. Numerical velocity fields in response to steady wind-forcing without rotation at the surface (a), at mid-depth $Z = 0.4$ (b) and one level above the bottom (c). The maximum velocity is 0.5122 m/s in (a), 0.0549 m/s in (b) and 0.1019 m/s in (c)

and $h < \delta$ for $W < 2$.

Plots of ε against n appear in Figures 17(a)–(d), for various values of W and K. Second-order convergence is apparent in all cases, as expected for equal-length linear elements. Generally higher K results in higher errors, with a limiting no-slip case realized at $K = 100$. At that limit the plots are easily explained by two rules:

(a) High frequency: for $W \geqslant 10$, ε depends on n alone, irrespective of W. Effectively the resolution of the skin-depth controls the error. In this range $n \geqslant 10$ provides $\varepsilon \leqslant 10^{-3}$.

(b) Low frequency: for $W \leqslant 3$, ε depends on m alone. This is apparent in Figure 17(d) from the half decade horizontal shift between $W = 1$ and $W = 0.1$, and is clarified in Figure 18 where ε is plotted against m. In this range the resolution of depth controls ε, and $m > 10$ provides $\varepsilon < 2.5 \times 10^{-3}$.
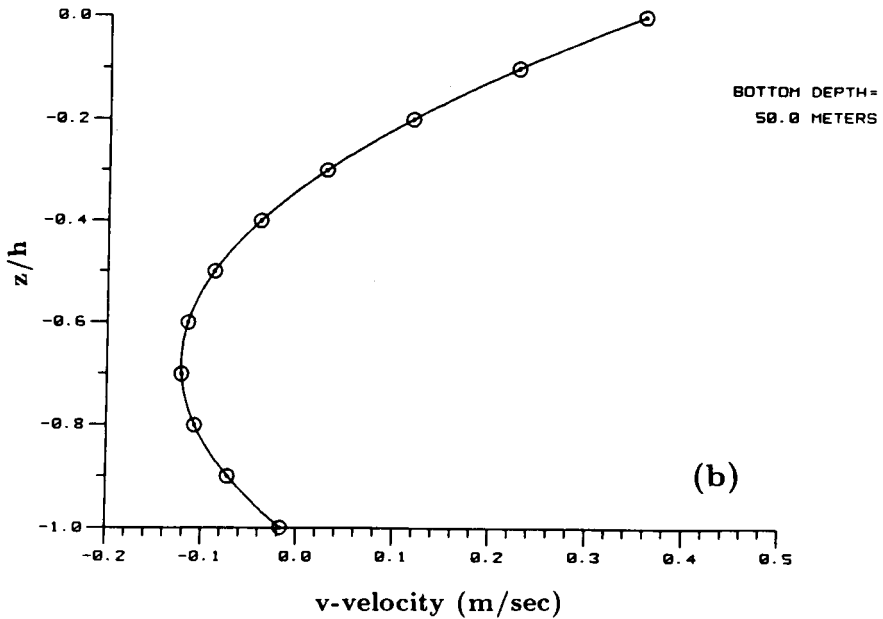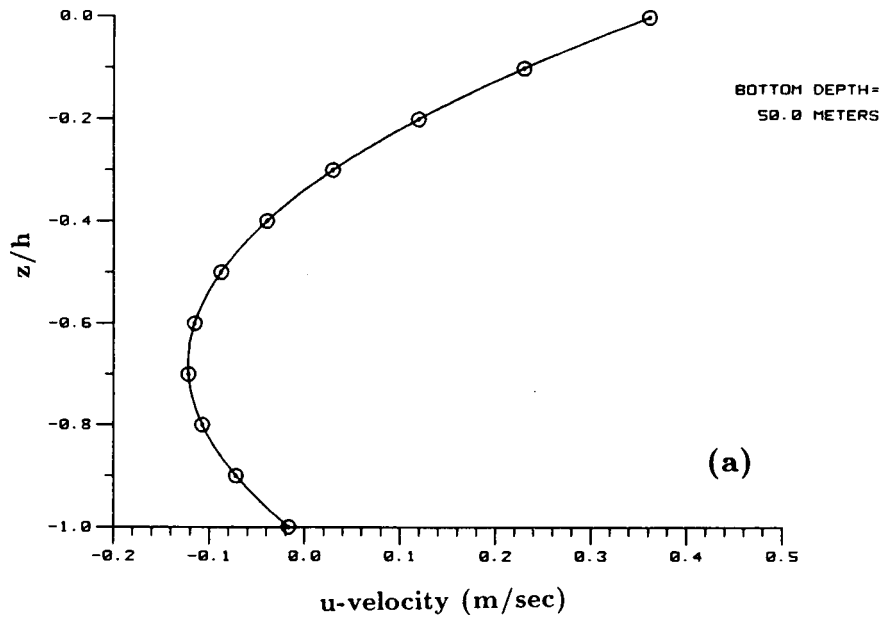
Figure 12. Analytic (solid lines) and numerical (circles) vertical profiles of velocity at mesh-point A (see Figure 5):
(a) u-component; (b) v-component
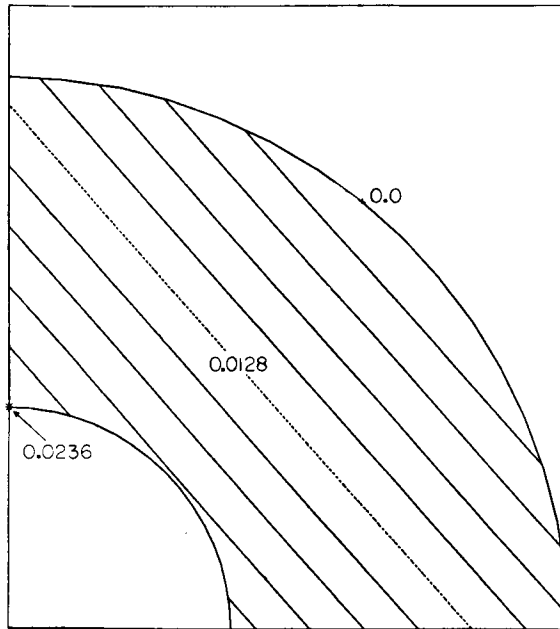
Figure 13. Elevation response (in metres) to steady wind forcing in the $\theta = 45°$ direction with rotation; Coriolis parameter evaluated for a latitude of 45°N
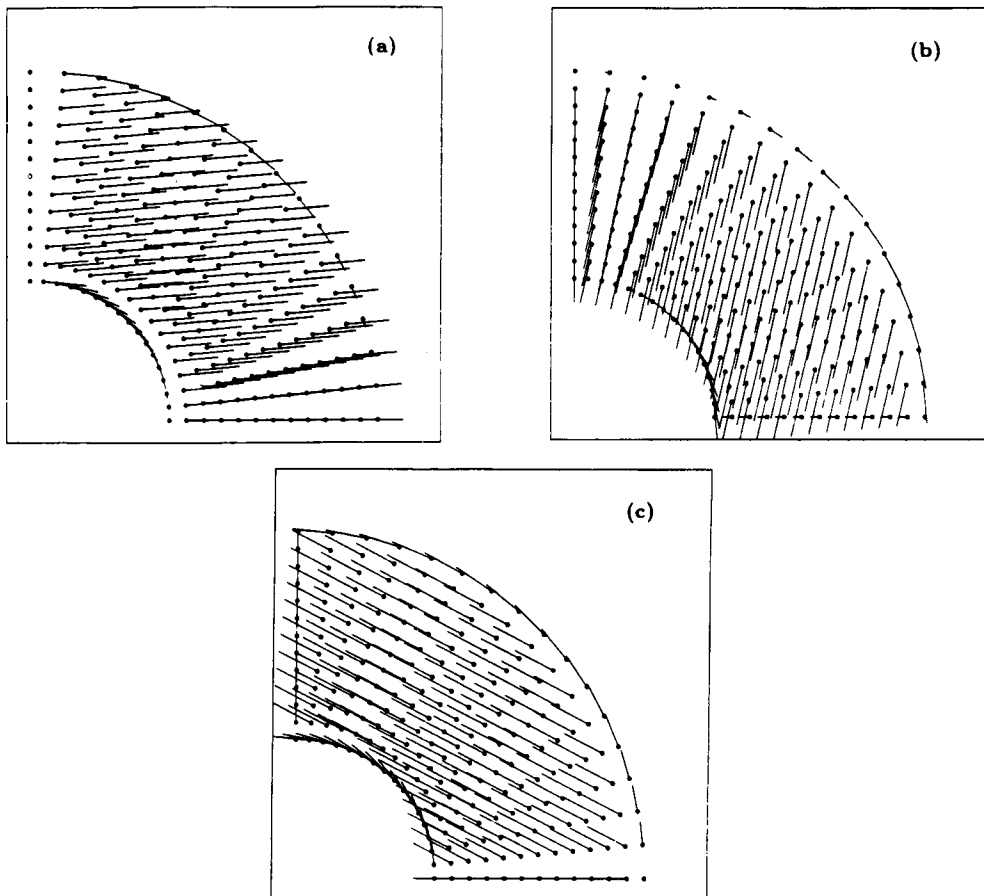
Figure 14. Numerical velocity fields in response to steady wind-forcing with rotation at the surface (a), level 3 below the surface $Z = 0.2$(b) and level 5 below the surface $Z = 0.4$(c). The maximum velocity is 0.1842 m/s in (a), 0.0319 m/s in (b) and 0.0271 m/s in (c)
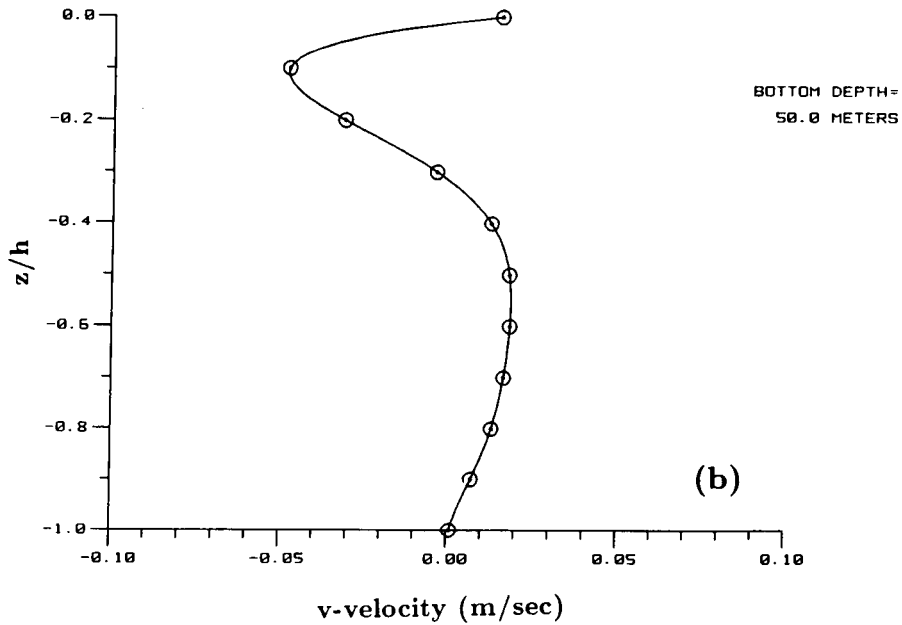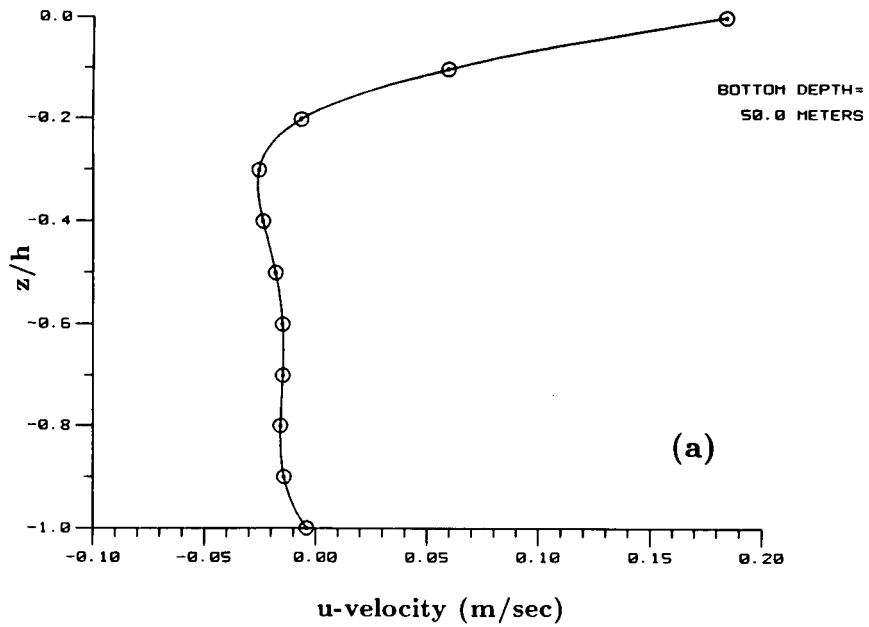
Figure 15. Analytic (solid lines) and numerical (circles) vertical profiles of velocity at mesh-point A for the steady wind-driven case with rotation (see Figure 5); (a) u-component; (b) v-component
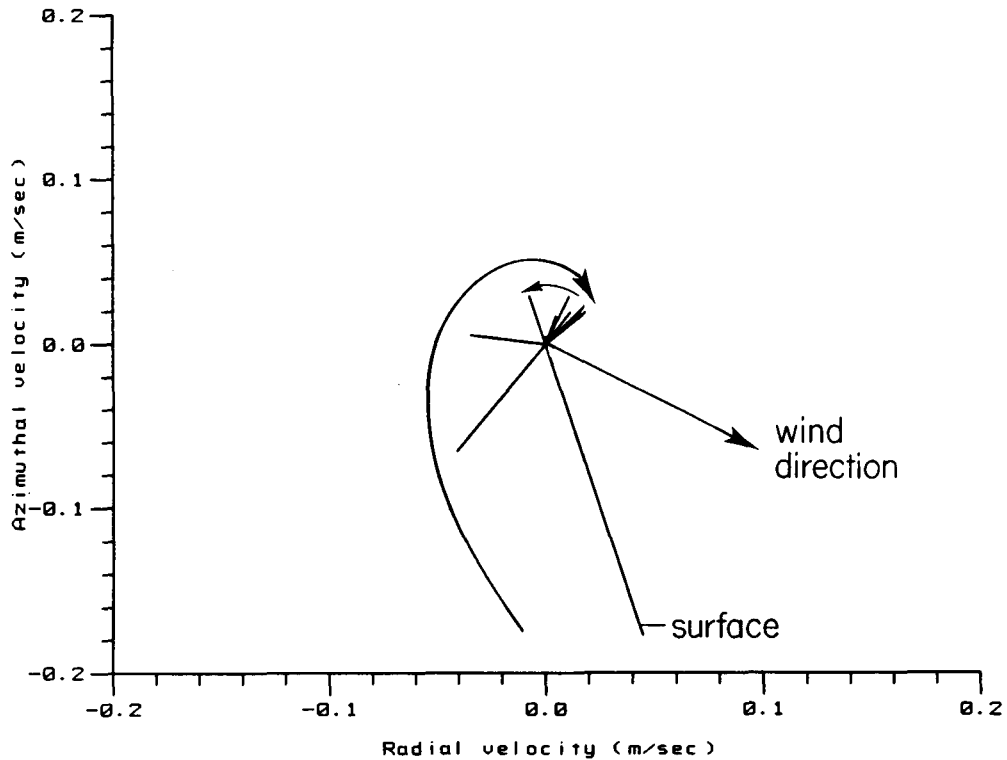
Figure 16. Hodograph of computed velocity at point A for the steady-wind case with rotation. The arrow indicates the direction of the current veering with depth. In the surface Ekman layer the veering is to the right of the wind direction (indicated by the clockwise arrows); at depth the veering in the bottom Ekman layer is to the left of the interior geostrophic velocity (in this case counterclockwise from the bottom).

Overall we obtain the simple gridding rules in Table I based on the worst-case, no-slip condition.

Table I. Vertical gridding rules

Discretization rules		
Max ε	Min $\delta/\Delta z$	Min $h/\Delta z$
10^{-2}	3	5
10^{-3}	10	16

TEST CASES: DISCRETE VERTICAL STRUCTURE

For the general case of variable $N(Z)$, we use the fully discretized model with computational steps as follows:

(a) Compute $P^{\pm}_{1,2}(Z)$ under each horizontal node using integral lumping on linear finite elements.

(b) Solve (45) for ζ. Identity (61) in the appendix may be used to avoid the averaging.

(c) Reconstruct $V_i(Z)$ beneath each node via (46) subject to the boundary conditions. Here $P^{\pm}_{1,2}$ are saved from the first step rather than recomputed.

Repetition of all the previous test cases using ten equal-spaced elements in Z produced
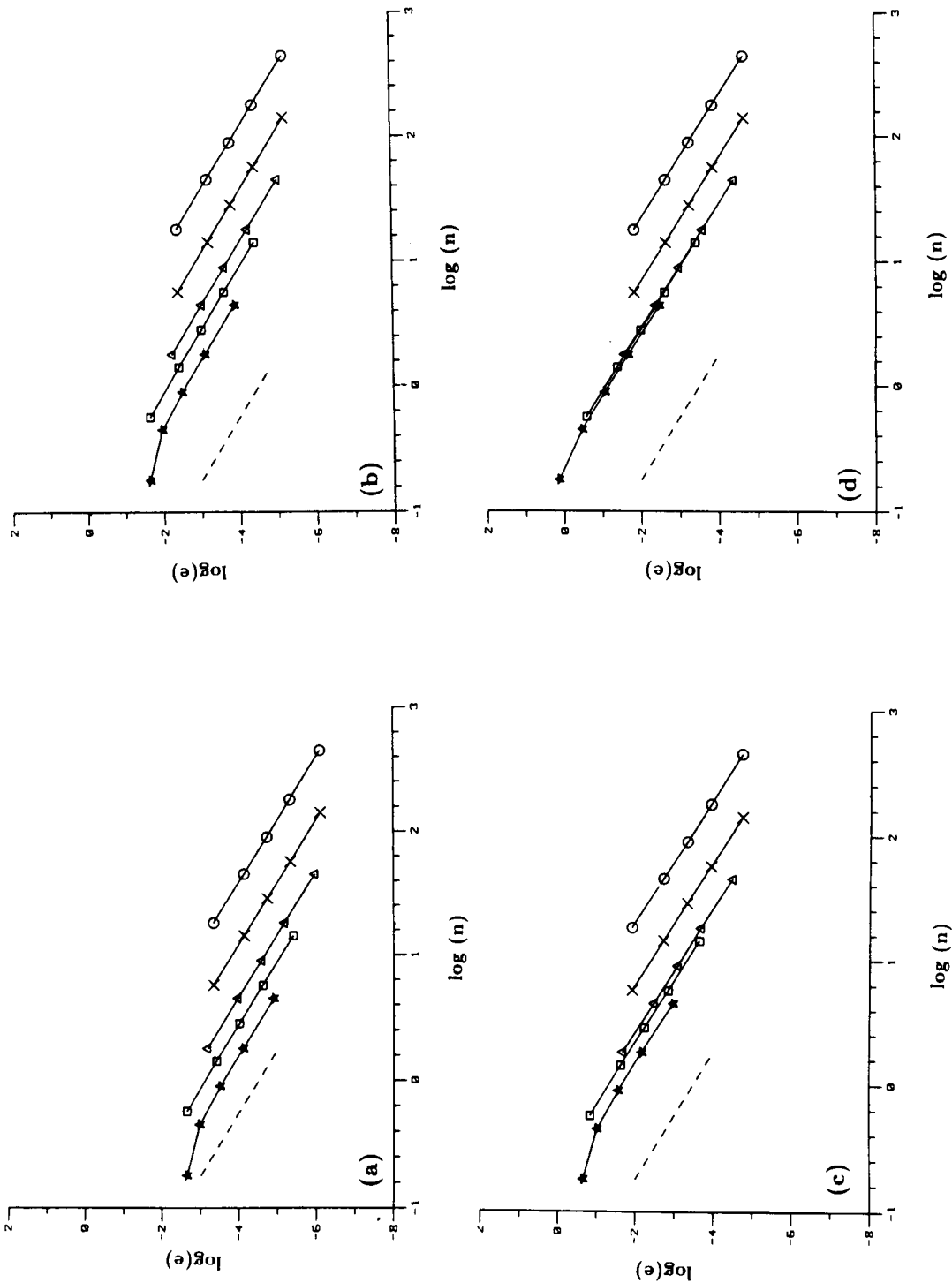
Figure 17. Error of the bottom stress parameter τ as a function of 'skin-depth' resolution for different values of W and (a) $K = 0.1$, (b) $K = 1.0$, (c) $K = 10.0$ and (d) $K = 100.0$. The curve with $\bigcirc$ corresponds to $W = 0.1$; the $\times$ to $W = 1.0$; the $\triangle$ to $W = 10.0$; the $\square$ to $W = 100.0$; and the $\bigstar$ to $W = 1000.0$. The dashed line has a slope of -2
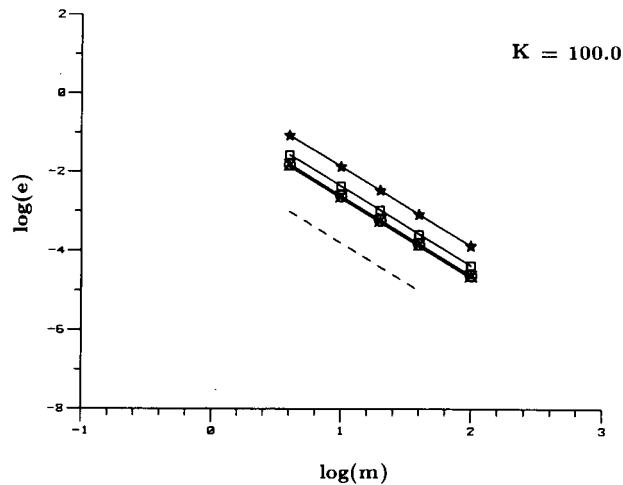
Figure 18. Error of the bottom stress parameter τ as a function of the number of nodes m in the vertical. The curve with $\bigcirc$ corresponds to $W = 0\cdot1$; the $\times$ to $W = 1\cdot0$; the $\triangle$ to $W = 3\cdot1$; the $\square$ to $W = 10\cdot0$; and the $\star$ to $W = 30\cdot0$. The dashed line has a slope of -2

practically indistinguishable results. An example of the more visible discrepancies appears in Figure 19.

For purposes of illustration, we discuss a final test involving a strongly stratified system in which there is no mixing across the pycnocline separating two otherwise homogeneous layers, i.e. $N = 0$ at mid-depth (Figure 20). In this example, we show the model's versatility in treating regions of high vertical shears by increasing the resolution in the region near the pycnocline. The forcing is due to the tide on the refined grid (Figure 5), with $\zeta_0 = \cos(2\theta)$ prescribed on the open boundary. The bathymetry is quadratic as defined earlier and h_0, k and ω are unchanged. Although the tidal amplitude over the domain is similar to that obtained in the case of constant N (compare Figures 21 and 4(c)), the difference in the velocity fields at different levels is quite marked (compare Figures 22, 23 and 24 to Figures 6, 8 and 9). Figures 22(a), (b) and 23 show that the flow in the surface layer is perfectly uniform, and does not feel the bottom, owing to the absence of momentum transfer (or vertical friction) between the fluid beneath and above the pycnocline. Lastly the spiral observed in Figure 9 is present only in the lower layer of the strongly stratified case (Figure 24).

FIELD APPLICATION: THE LAKE MARACAIBO SYSTEM

In this section we discuss some results of the methods presented thus far applied to a realistic situation, specifically to the Lake Maracaibo (LM) system. The LM system is located in the north-west corner of Venezuela (see Figure 25) and is composed of 4 smaller bodies of water: (i) the Gulf of Venezuela which is approximately 180 km long and 75 km wide and averages 30 m in depth; (ii) the Bay of El Tablazo which is 27 km × 24 km and averages 2.5 m in depth; (iii) the Strait which is 37 km long × 10 km wide and 10 m deep; and (iv) Lake Maracaibo itself which is 120 km long (north–south) and 110 km wide (east–west), averaging 25 m in depth.

Studies of the semi-diurnal tidal regime in the LM system have uncovered a behaviour resembling that of a standing wave produced by the propagation of the tide through the Gulf of Venezuela and reflecting from the head of the Lake. Although the tides in the Caribbean (in the area of Cuba, Santo Domingo, Puerto Rico and the Venezuelan coast) are mixed but predominantly *diurnal*, the measurements at the mouth of the Bay of El Tablazo indicate that the tide there is still mixed but predominantly *semi-diurnal*. This phenomenon has been recognized as a resonance
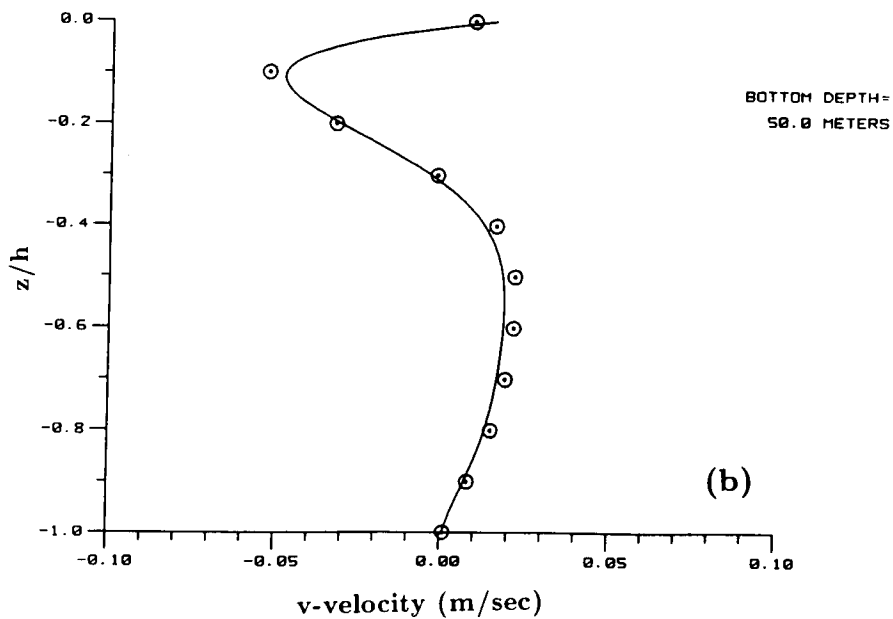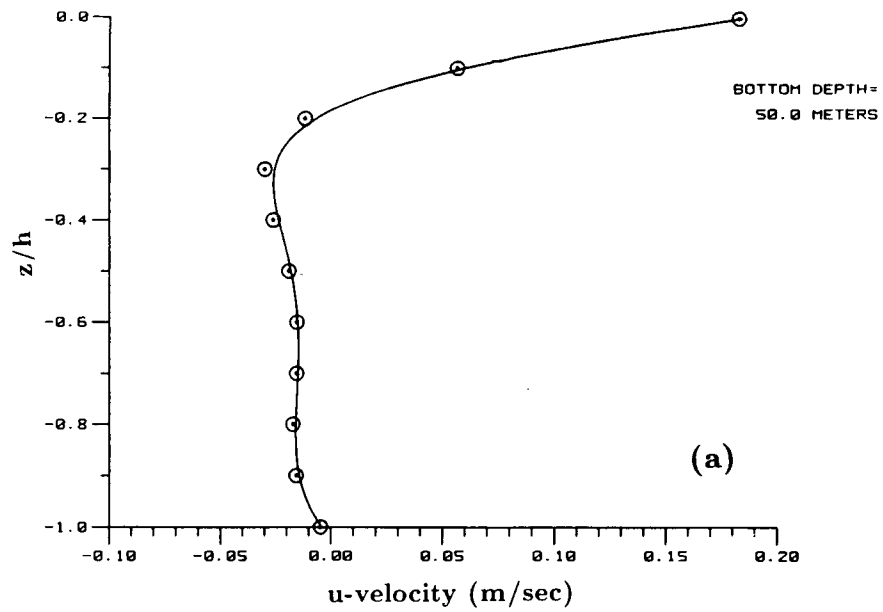
Figure 19. Comparison of a fully analytical solution for the steady wind-driven case with rotation and fully numerical solution, in which the vertical is solved on finite elements: (a) u-velocity; (b) v-velocity. Compare with Figure 15, where the vertical was treated analytically
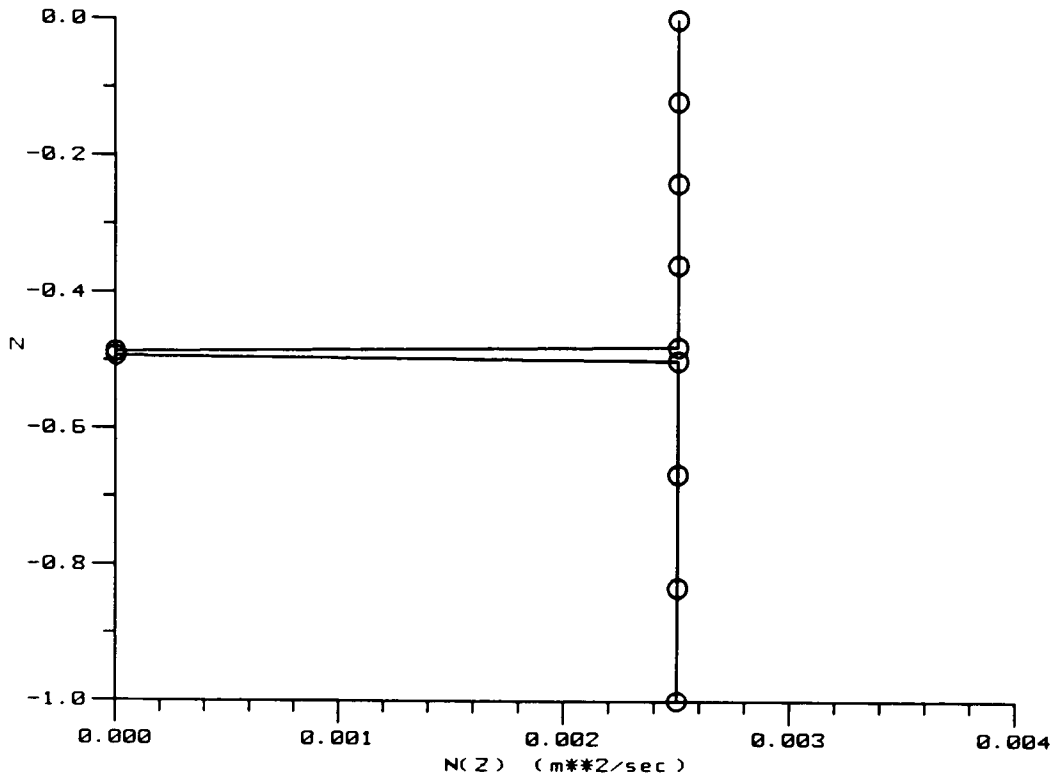
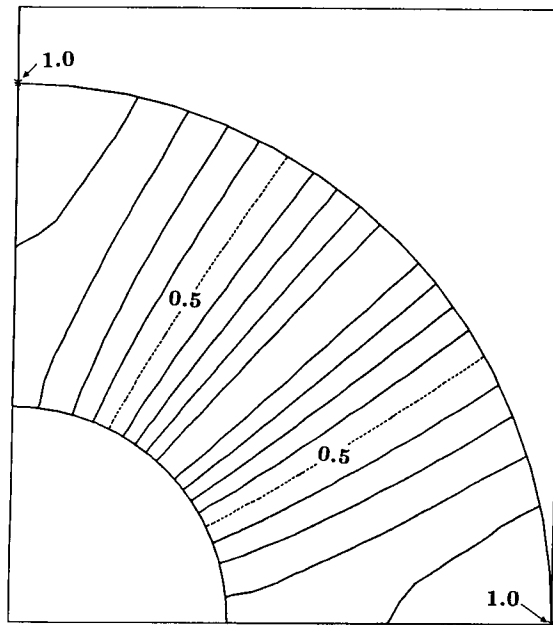Figure 20. Vertical profile of the depth-dependent vertical eddy viscosity

Figure 21. Numerically computed tidal amplitude with depth-dependent vertical eddy viscosity. The contour interval is 0·1 m. The prescribed tidal amplitude on the open boundary is $\zeta_0 = \cos(2\theta)$
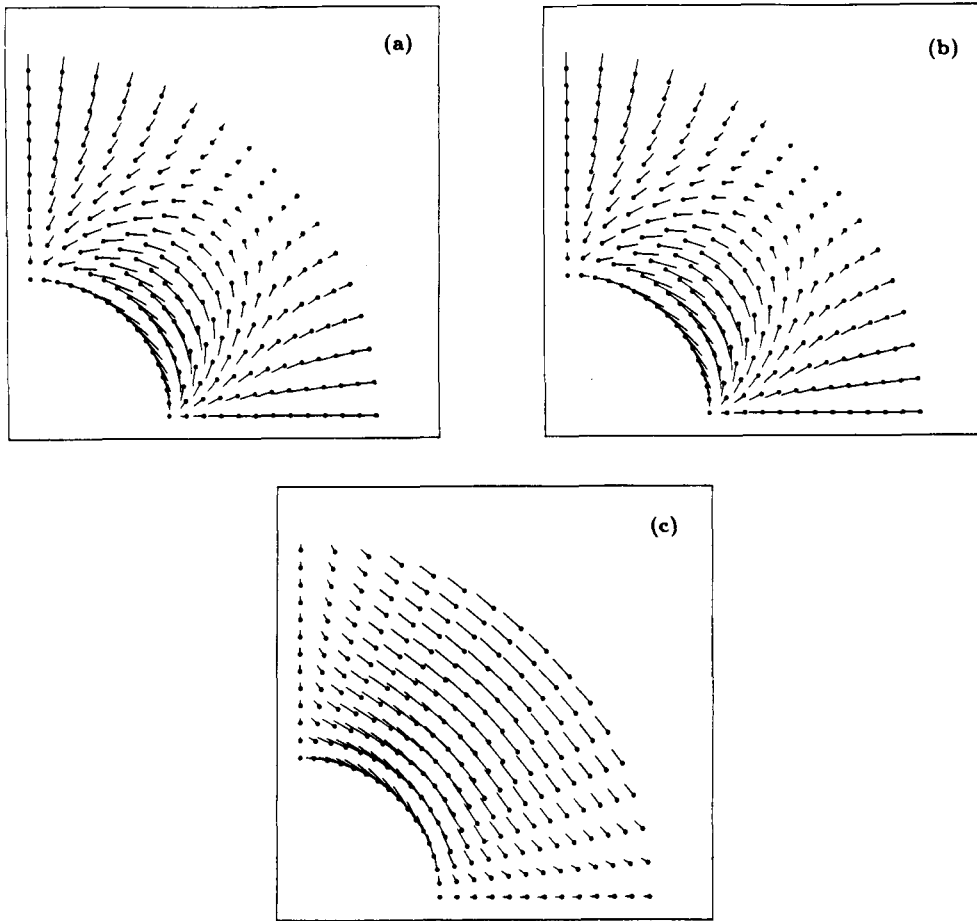
Figure 22. Numerical velocities at $t = 0$ forced by $\zeta_0 = \cos(2\theta)$ with depth-dependent viscosity at the surface (a), at mid-depth $Z = 0\cdot4$ (b) [identical to (a)] and one level above the bottom (c). The maximum velocity is $0\cdot3584$ m/s in (a), $0\cdot3584$ m/s in (b) and $0\cdot3946$ m/s in (c)

effect on the semi-diurnal tides induced by the dimensions of the Gulf of Venezuela.[24,25] Specifically, the amplitude of the M_2 component grows from 10 cm at the entrance to the Gulf, to 41 cm at EI Tablazo Bay. The tide retains its semi-diurnal character across EI Tablazo and the Strait of Maracaibo. High water is felt almost synchronously along this stretch, is delayed by about 1 h relative to the high water in the Gulf and has a range that diminishes progressively to the south. Whereas at the northern end of the Lake the tides are greatly reduced, at the southern end the semi-diurnal character of the tide is restored, its amplitude increasing to 3–4 cm. The observed time of high water at that point is 6 h after high water in the Gulf of Venezuela, i.e. about 180° out of phase for the M_2 tide.

The mesh used in our studies of the LM system is shown in Figure 26 and contains 718 elements and 433 nodes. Two cases are considered: (i) a tidal case where a constant amplitude (10 cm) M_2 tide with a 10° linearly varying phase is prescribed across the north-eastern seaward boundary of the Gulf of Venezuela (the western side leading[25]) and (ii) the steady, wind-driven circulation due to a north-easterly wind. No-normal-flow conditions were imposed on the solid boundaries, and the bottom bathymetry is that shown in Figure 25.
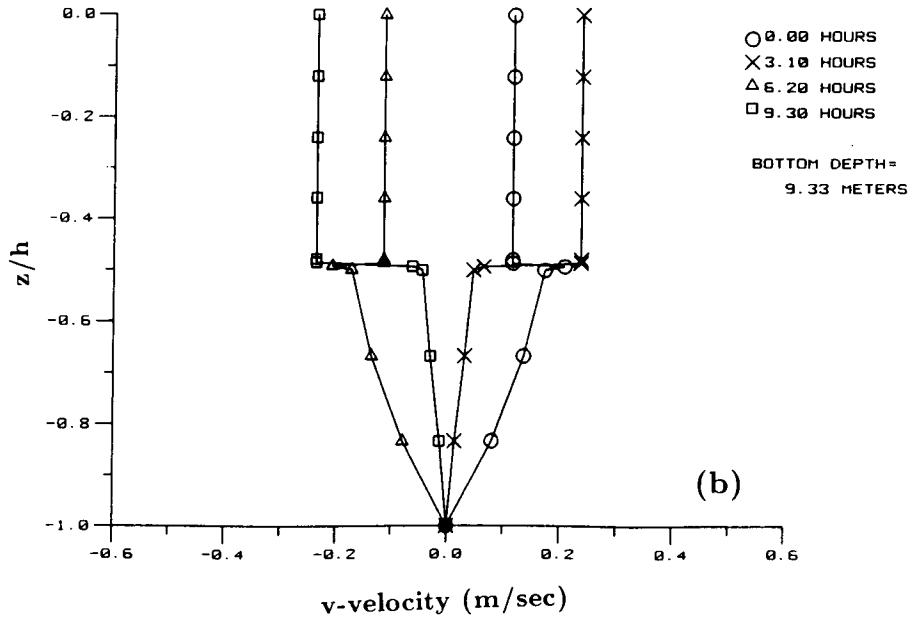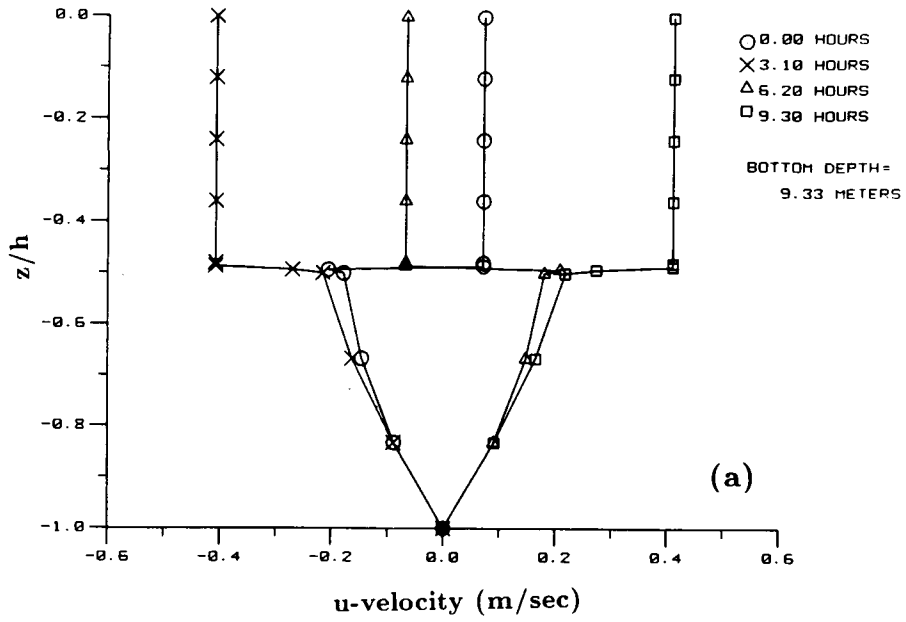
Figure 23. Computed profiles of velocity for the case of depth-dependent viscosity at four times in the tidal cycle at mesh-point A(see Figure 5): (a) u-component; (b) v-component
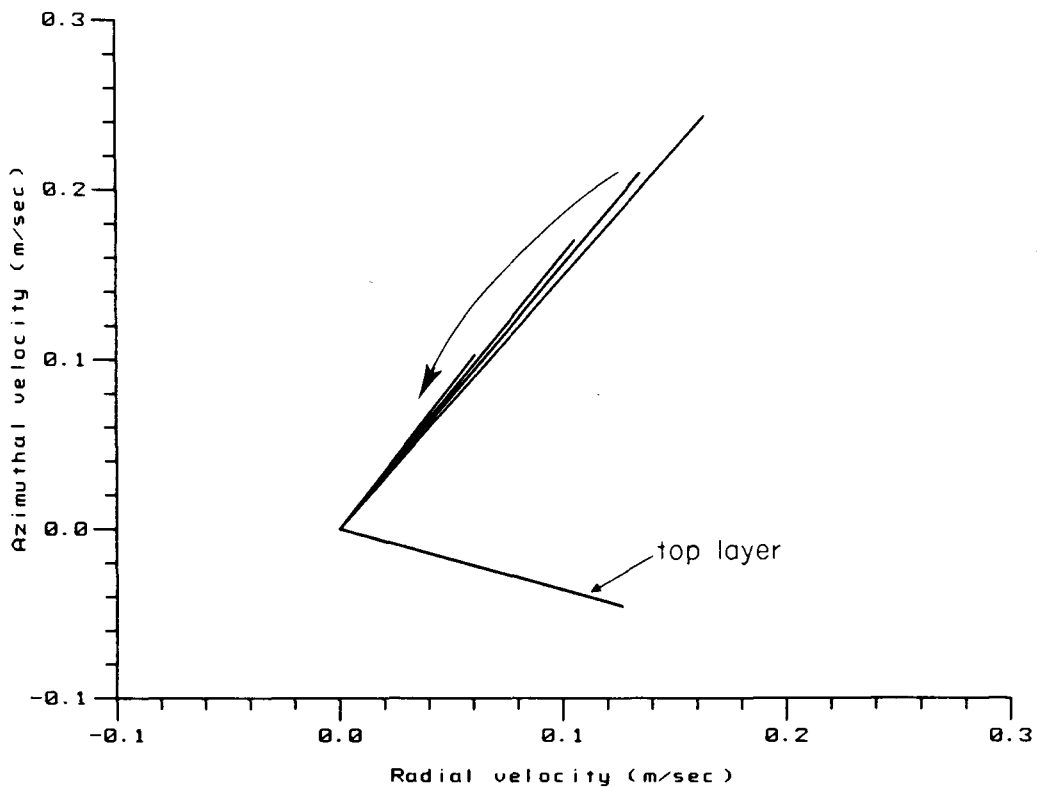
Figure 24. Hodograph of velocity at point A at $t = 0$ for depth-dependent viscosity. The arrow indicates the direction of the current veering with depth (from mid-depth to bottom). Note that the surface layer velocities are uniform in direction and magnitude and the veering with depth in the lower layer (refer to Figure 23)

In all cases the bottom slip coefficient k was 0.002 m/s, and 11 equally spaced nodal points were used to resolve the vertical direction. Since h varies with (x, y) so also does Δz. In the Figures that follow we show the flow at the surface nodes and the nodes immediately *above* the bottom-most node; for brevity we will call this latter level the bottom level.

Tidal response

First, we present results from the M_2 tidally forced flow, with constant $N(= 0.0025 \text{ m}^2/\text{s})$ and analytic solutions for the vertical structure (as in the test cases, the numerical treatment of the vertical showed no noticeable difference). The expected resonance of the tide in the Gulf of Venezuela and its overall amplitude were reproduced (Figure 27). Also, the phase of the response (Figure 28) showed the observed 180° shift between the Gulf and the Lake, as well as the amphidrome just south of the Strait of Maracaibo found by Molines and Fornerino.[25] Both the observed and the model tidal amplitudes decrease in the Strait of Maracaibo and are under 5 cm in the Lake itself. Currents 6·2 h after the high tide at the open boundary are shown in Figures 29 (top level) and 30 (bottom level). At this time, the currents are flowing seaward in the Gulf and into the Lake in the Strait. The highest currents occur in the Bay of El Tablazo and the Strait of Maracaibo and can be greater than 50 cm/s; the smallest tidal currents are found in the Lake itself and are of the
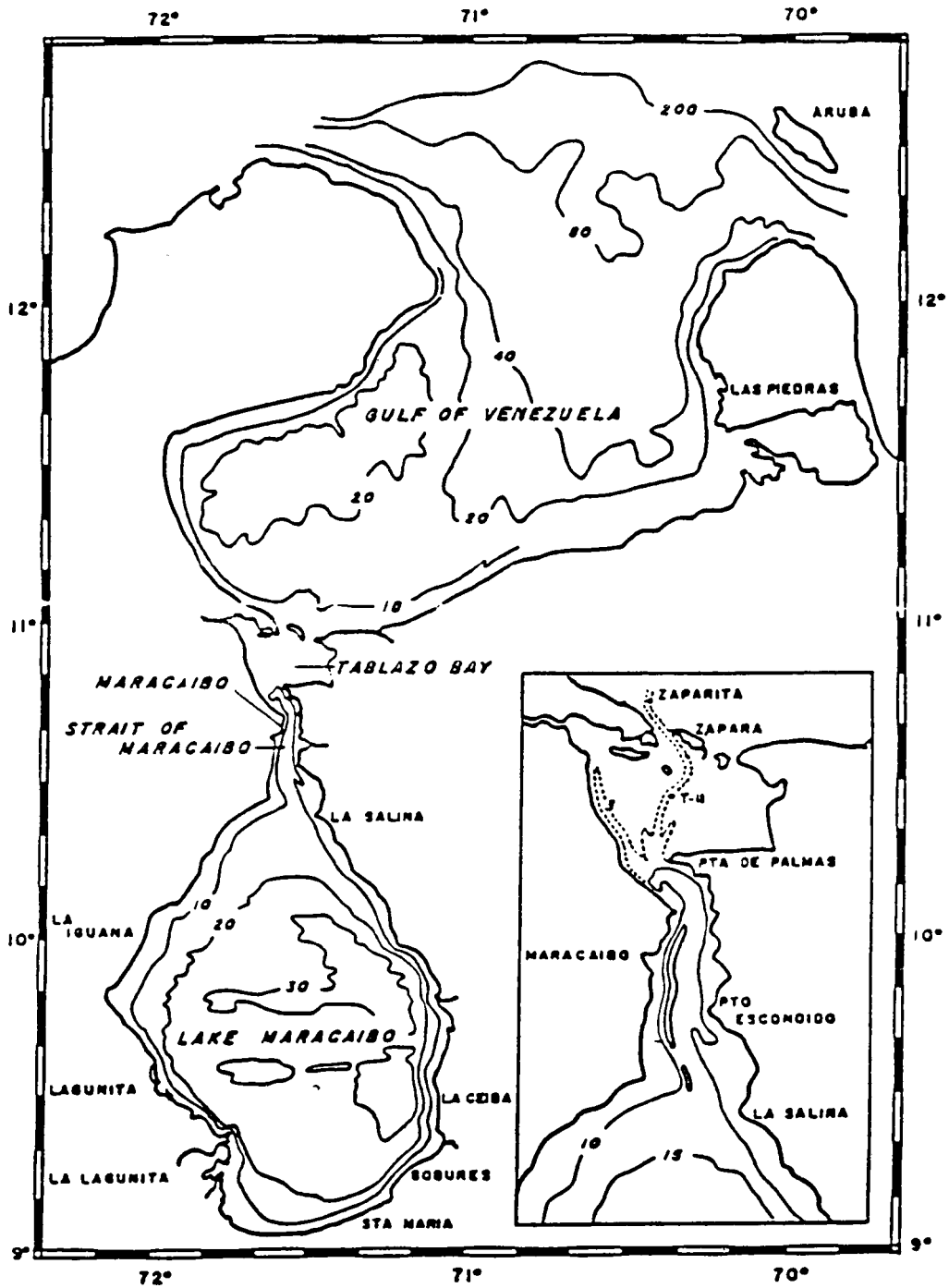
Figure 25. Topography and place names of the Lake Maracaibo system taken from Reference 24. The depth contours are in metres
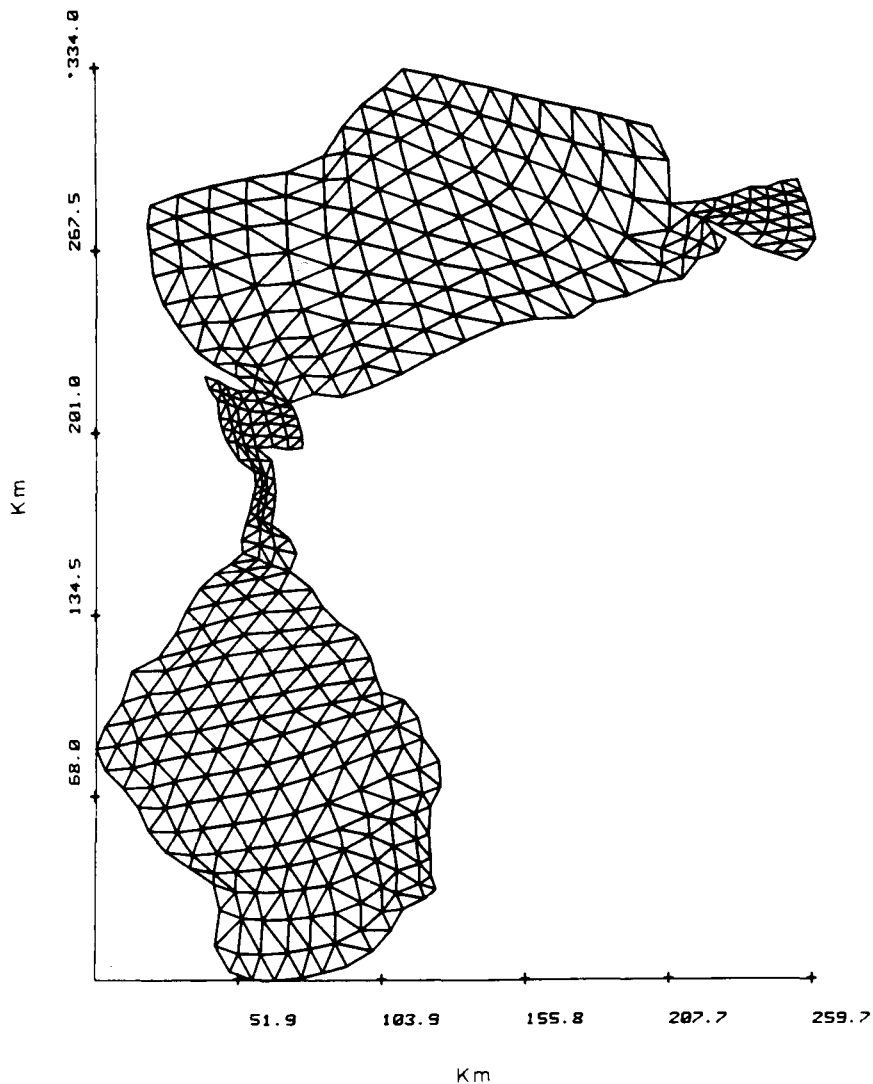
Figure 26. Mesh used in the Lake Maracaibo system studies with 433 nodes and 718 elements

order of 2–5 cm/s. A reduction in magnitude with depth is seen in the velocity (largest velocities of the order of 20–30 cm/s). The flow patterns agree with the observed anti-node of the M_2 tide located in the Bay of EI Tablazo. Thus in this region, the convergence and divergence of the M_2 tidal currents causes the above mentioned circulation features, in which flows south of EI Tablazo Bay may be *southward* at the same time that the flows in the passages from the Gulf of Venezuela to EI Tablazo Bay are *northward* (Reference 26, Figure 7).

Figures 31 (top level) and 32 (bottom level) show the tidal velocities at the surface and at the bottom, 3·1 h into the tidal cycle (after the high tide on the open boundary). This point in time shows that in addition to the decrease in magnitude between the surface and the bottom, there can be a reversal in the flow direction between the two levels at certain locations. Runs with a depth-dependent but continuous N presented generally similar features and are not shown.
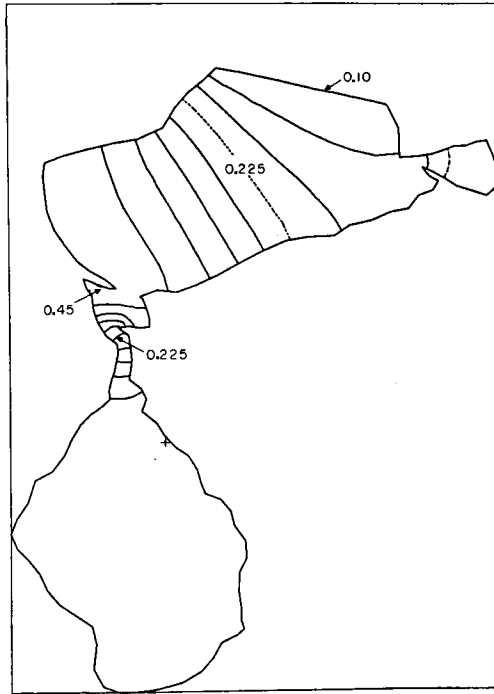
Figure 27. Amplitude response for the M_2 tide. Location of the + indicates position of the minimum amplitude. Elevation in metres, the contour interval is 0·042
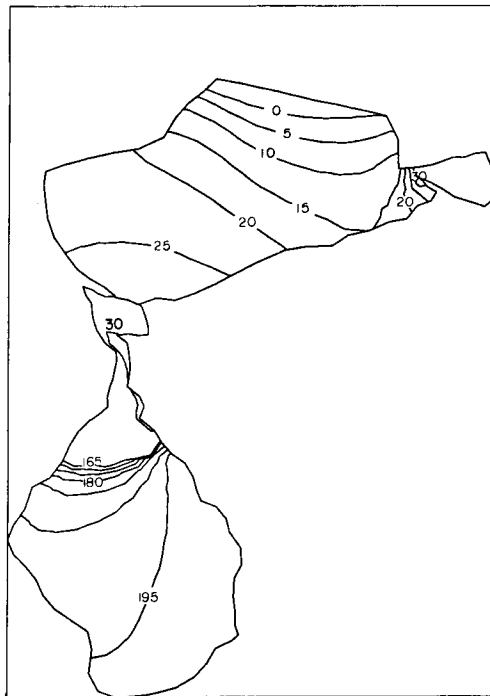

Figure 28. Phase response of the M_2 tide. The wave propagation about the amphidrome is counterclockwise. Refer to Figure 27 for the position of minimum tidal amplitude. The contour interval is 5°
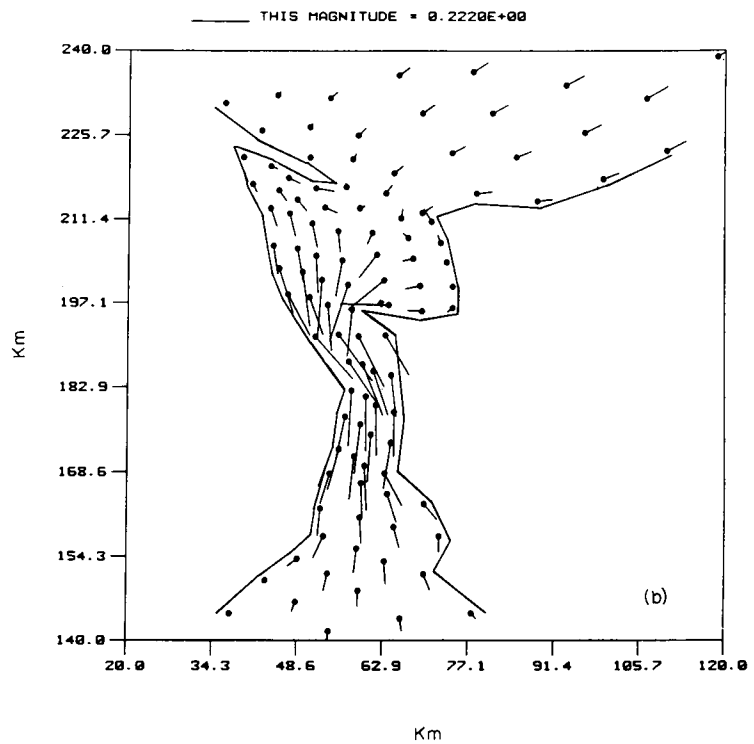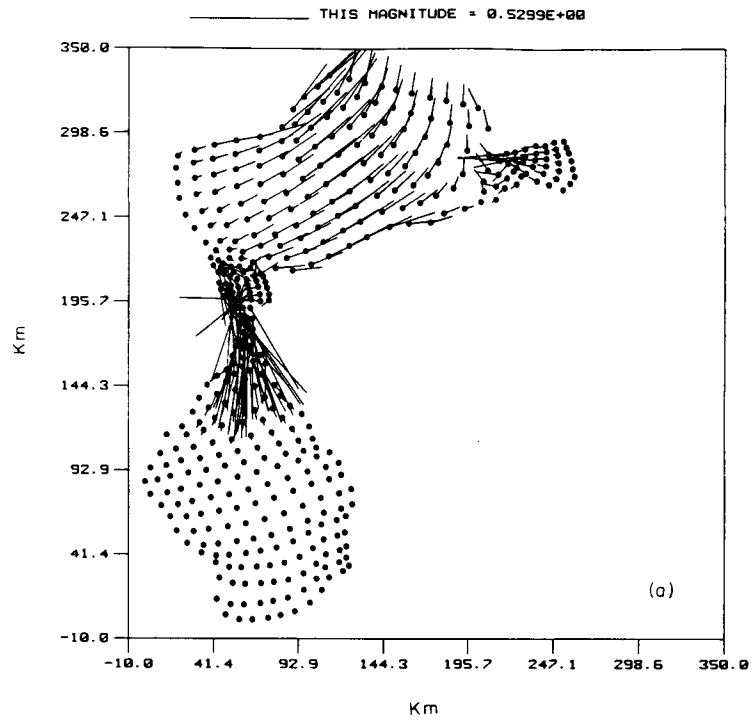
Figure 29. Tidal currents of top level 6·2 h into the tidal cycle with the constant N. Entire Lake Maracaibo system (a), and detail of EI Tablazo Bay and Maracaibo Strait (b). Velocity magnitude in m/s. Here and subsequently the boundary is offset slightly from the actual position on the nodes to enhance the display
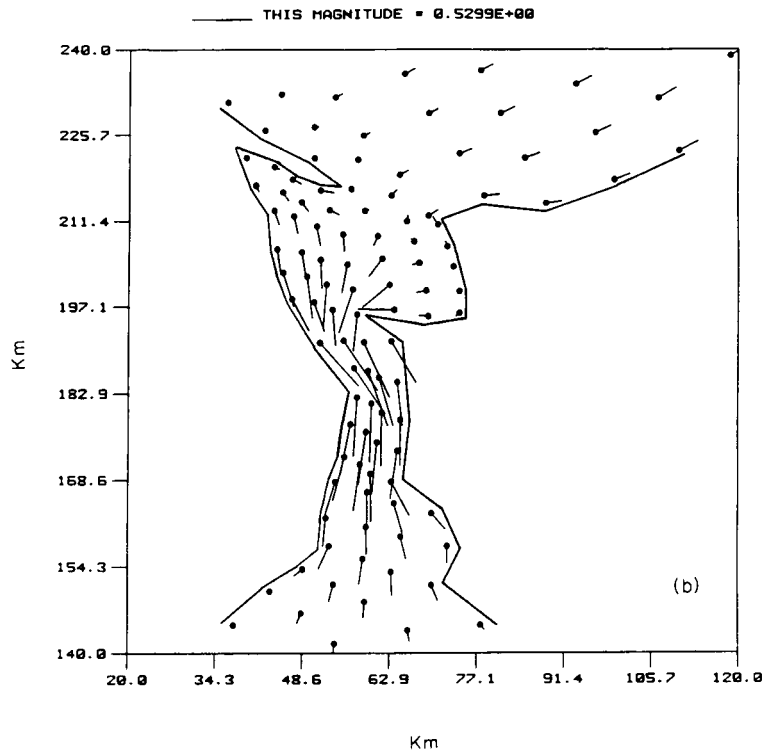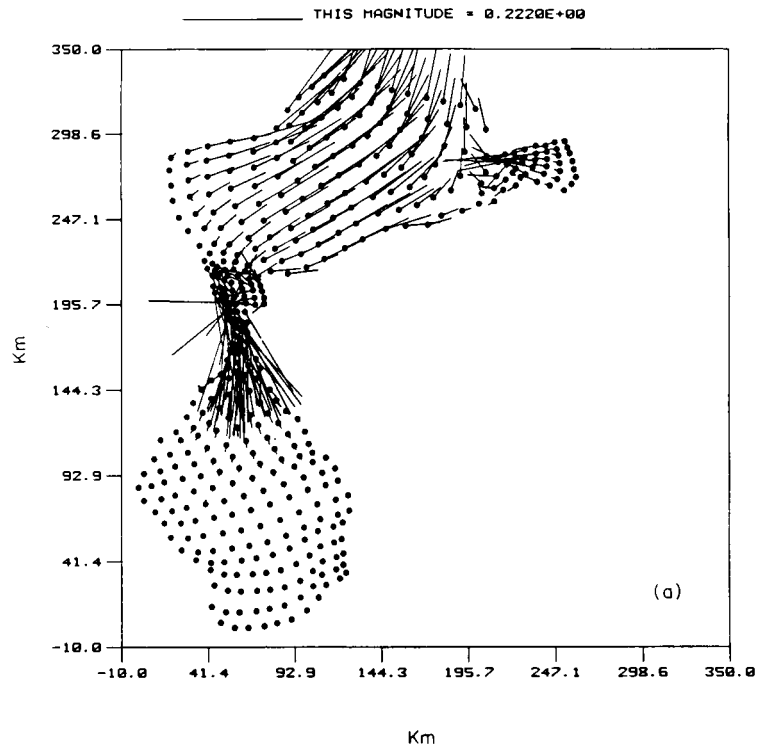
Figure 30. Tidal currents one level above the bottom 6·2 h into the tidal cycle with constant N. Entire Lake Maracaibo system (a), and detail of EI Tablazo Bay and Maracaibo Strait (b). Velocity magnitude in m/s

Figure 31. Tidal currents of top level 3·1 hours into the tidal cycle with constant N. Entire Lake Maracaibo system (a), and detail of EI Tablazo Bay and Maracaibo Strait (b). Velocity magnitude in m/s

Figure 32. Tidal currents one level above the bottom 3·1 hours into the tidal cycle with constant *N*. Entire Lake Maracaibo system (a), and detail of EI Tablazo Bay and Maracaibo Strait (b). Velocity magnitude in m/s
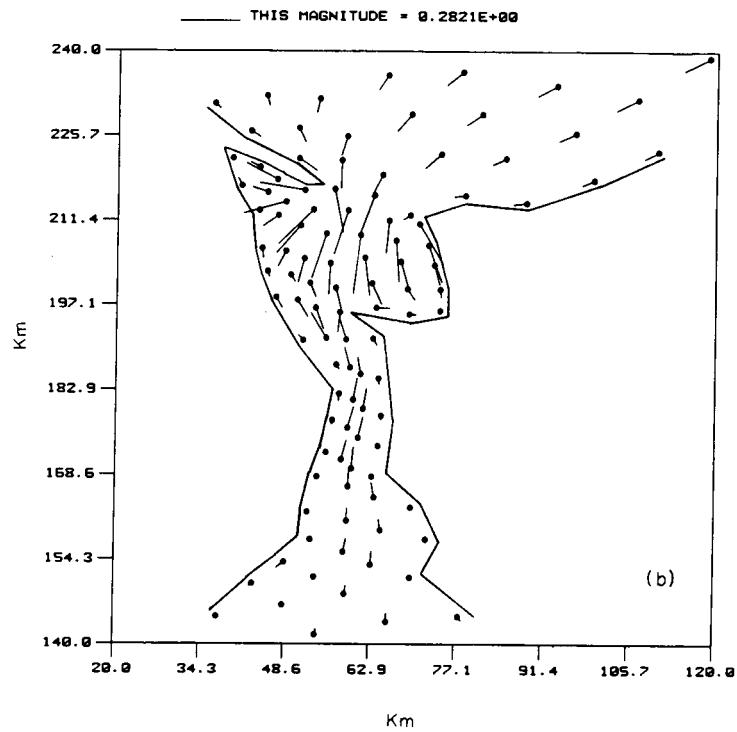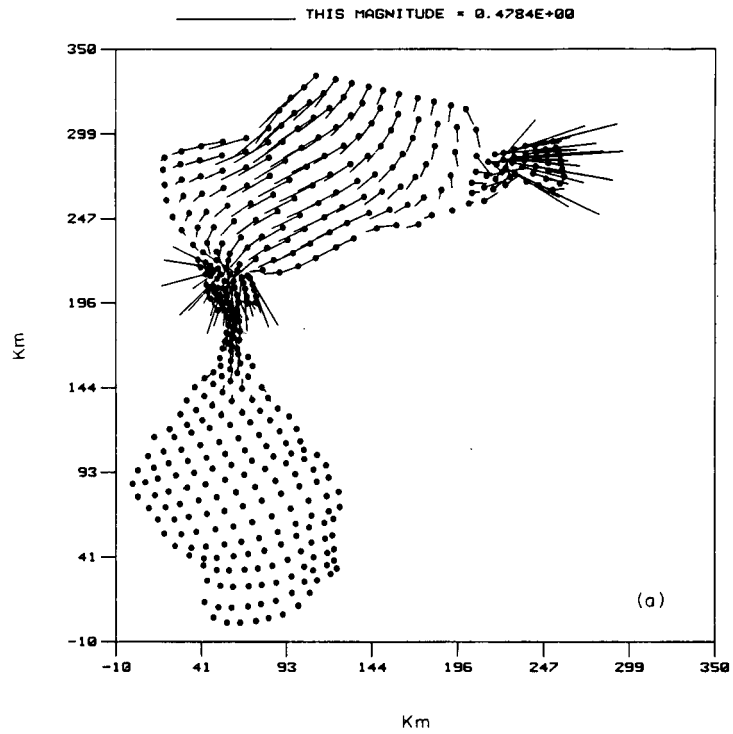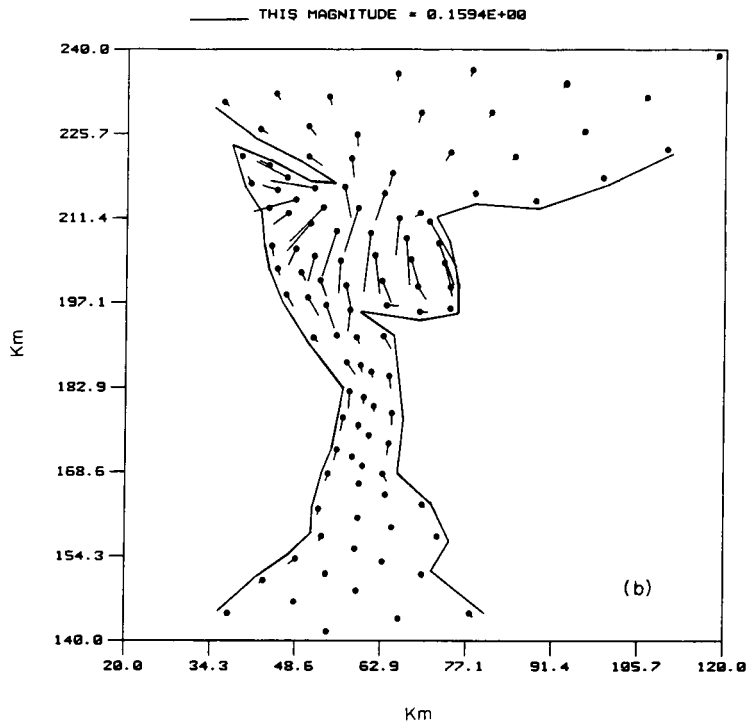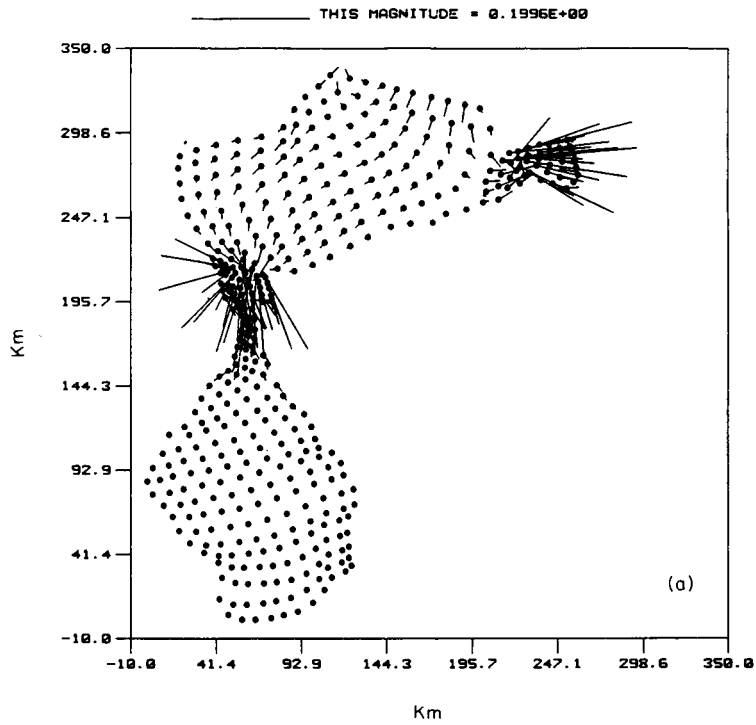
Steady wind-driven flow

The model results for the steady wind-forced case with a north-easterly wind of magnitude 1 dyne/cm^2, constant $N(= 0\cdot0025\,m^2/s)$ and analytic vertical structure are shown in Figures 33(a), (b) and (c). The seaward boundary was fixed at $\zeta = 0$. The difference between the depth-averaged velocity field (Figure 33(a)) and the flow in the surface and bottom layers (Figures 33(b) and (c)) is striking. Note that, whereas the mean flow shows a recirculating gyre in the region of the Gulf and the Lake itself, the surface velocities follow the direction of the wind stress and the bottom flow is directed opposite to the surface velocity field. Measurements by Parra-Pardi *et al.*[27] show the counterclockwise circulation in the Lake, and Zeigler[28] infers a counterclockwise circulation for the Gulf of Venezuela.
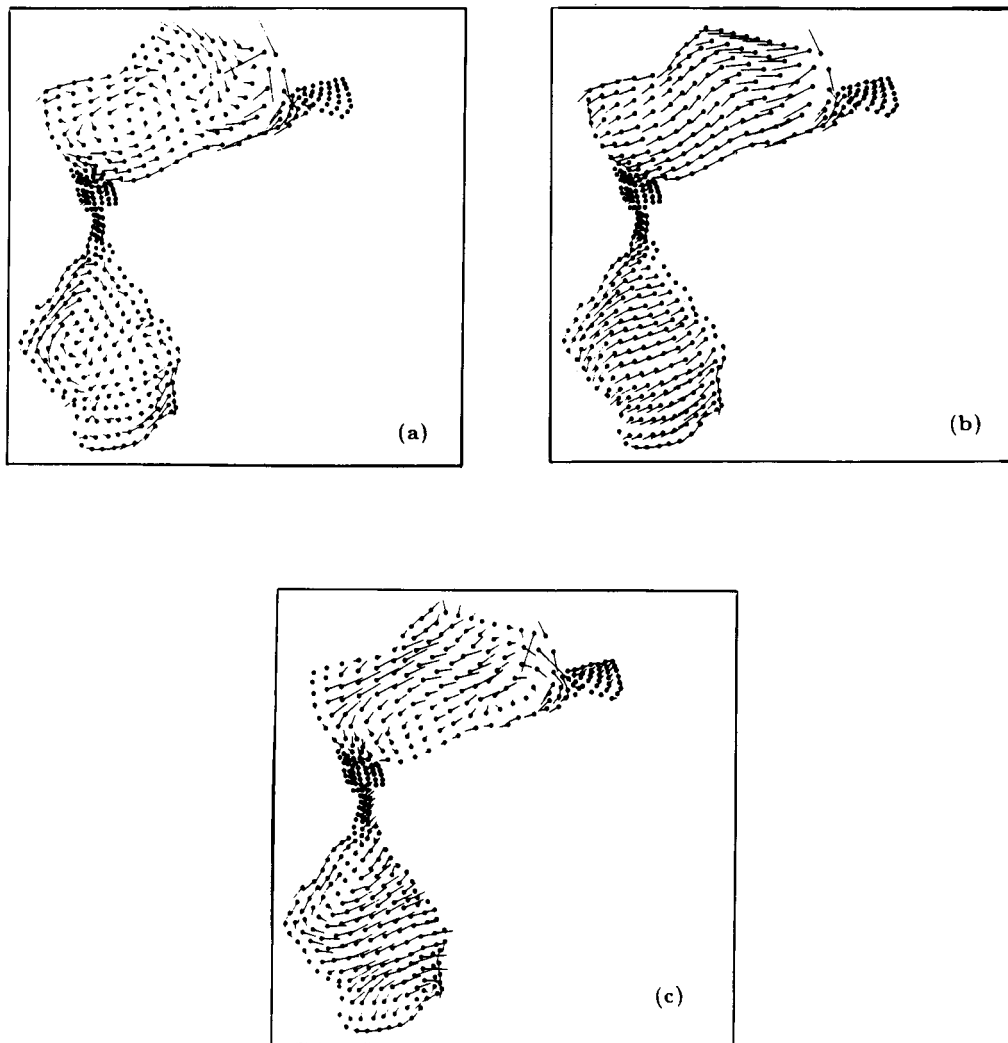

Figure 33. Steady state current response to north-easterly winds of 1·0 dyne/cm^2 with constant N. Vertically averaged velocity (a), top level (b) and one level above the bottom (c). The maximum velocity is 0·2631 m/s in (a), 0·6428 m/s in (b) and 0·1518 m/s in (c)

SUMMARY AND DISCUSSION

The model presented here provides full three-dimensional solutions for linearized periodic hydrodynamics. It is useful as a diagnostic tool, as a predictive tool within the limits of the linearization; and as an initial condition generator for non-linear time-stepping models. Methodologically the model synthesizes established and cost effective concepts for solving the vertically averaged equations with a simple and general approach to the representation of the vertical. From an economical standpoint the model requires only a two-dimensional Helmholtz solution for a single scalar unknown, plus a number of tridiagonal solutions. Accuracy relative to analytical solutions is very satisfying with reasonably coarse meshes. The interchangeability of the analytic and numerical vertical representation is especially appealing, and the more general numerical option creates no major penalty in run time, memory or accuracy provided that the simple gridding rules are observed.

A considerable portion of the most dominant observed features of the M_2 tide in the LM system has been explained by this model. The model tidal amplitude, its propagation through the system and the predicted velocities all agree with available field measurements: these include the resonance in the Gulf of Venezuela, the nodal and antinodal line in the Bay of El Tablazo, the phase difference between the Gulf and the Lake (including the occurence of the amphidromic point in the Lake). Similarly, the wind-driven gyres in the two main basins of the system are captured by the model. Further comparisons with flow and sea-level measurements is limited at this time since in reality additional effects due to stratification and other non-linear processes will also have to be taken into account. A complete treatment of some of these effects is under way and will be the subject of a forthcoming paper.

APPENDIX

Here we record some identities relative to the vertical structure and the bottom stress which are useful when $\omega \neq 0$. Starting with the homogeneous form of equation (9),

$$j\omega\mu_{1,2} - \frac{d}{dZ}\left(\frac{N}{h^2}\frac{d\mu_{1,2}}{dZ}\right) = 0, \tag{56}$$

we integrate from $Z = -1$ to $Z = 0$, to obtain

$$\bar{\mu}_{1,2} = \frac{N}{j\omega h^2}\dot{\mu}_{1,2}\Big|_{-1}^{0}. \tag{57}$$

Equation (57) may be used to eliminate the need for $\bar{\mu}$ in expressions (24) and (25) for τ and α, such that only μ and $\dot{\mu}$ need be evaluated. The identity (57) also governs numerical solutions to (56) obtained by any weighted residual method of the form

$$\int_{-1}^{0} j\omega\mu\phi_i \, dZ + \int_{-1}^{0} \frac{N}{h^2}\frac{d\mu}{dZ}\frac{d\phi_i}{dZ} \, dZ - \frac{N}{h^2}\frac{d\mu}{dZ}\phi_i\Big|_{-1}^{0} = 0 \tag{58}$$

provided that the weighting functions sum to unity everywhere (as in most common Galerkin finite

element solutions). This can be seen by summing all of the equations (58), in which case $\sum \phi_i \to 1$, and $\sum (\mathrm{d}\phi_i/\mathrm{d}Z) \to 0$, and identity (57) follows. Use of (57) yields an additional identity among the B and A matrices defined in equations (14) and (15):

$$B - A(-1) = \frac{j\omega \bar{A}h}{k}.$$ (59)

Thus the expression (24) for τ may be equivalently stated as

$$\tau = \frac{j\omega \bar{A}}{B - A}.$$ (60)

Similar properties may be derived in the same way for $P_1(Z)$ and $P_2(Z)$ whether obtained analytically or by a weighted residual method with $\sum \phi_i = 1$:

$$\bar{P}_{1,2} = \frac{1}{j\omega}\left[1 - \frac{k}{h}P_{1,2}(-1) \right].$$ (61)

Thus equations (21) and (22) may be expressed equivalently:

$$\tau = j\omega\left[\frac{kP_1(-1)/h}{1 - kP_1(-1)/h} \right],$$ (62)

$$\alpha = \frac{\tau}{j\omega}\left[1 - \frac{k}{h}P_2(-1) \right] - \frac{k}{h}P_2(-1),$$ (63)

and the need to compute $\bar{P}_{1,2}$ is eliminated.

REFERENCES

1. C. E. Pearson and D. F. Winter, 'On the calculation of tidal currents in homogeneous estuaries', *J. Phys. Oceanography*, 7(4), 520–531 (1977).
2. C. Le Provost and A. Poncet, 'Finite element method for spectral modelling of tides', *Int. j. numer. methods eng.*, 12, 853–871 (1978).
3. B. M. Jamart and D. F. Winter, 'Finite element computations of the barotropic tides in Knight Inlet, British Columbia', in H. J. Freeland, D. M. Farmer and C. D. Levings (eds), *Fjord Oceanography*, Plenum Press, New York, 1980, pp. 283–289.
4. R. A. Walters, 'Finite element solution methods for circulation in estuaries', in J. P. Laible, C. A. Brebbia, W. Gray and G. Pinder (eds), *Proc. 5th Int. Conf. on Finite Elements in Water Resources*, Springer-Verlag, Berlin, 1984, pp. 587–596.
5. D. R. Lynch, 'Comparison of spectral and time-stepping approaches for finite element modeling of tidal circulation', in *Proceedings Oceans 81, IEEE Pub. No. 81CH 1685-7:810-814*, Boston, MA, 1981.
6. D. R. Lynch, 'Mass balance in shallow water simulations', *Comm. in Appl. Num. Methods*, 1, 153–159 (1985).
7. A. F. Blumberg and G. Mellor, 'A description of a three-dimensional coastal ocean circulation model', in N. Heaps (ed.), *Three-Dimensional Shelf Models, Coastal and Estuarine Sciences*, 5, American Geophysical Union, 1985.
8. A. M. Davies, 'A three-dimensional model of the northwest European continental shelf, with application to the M_4 tide', *J. Phys. Oceanography*, 16(5), 797–813 (1986).
9. N. S. Heaps and J. E. Jones, 'A three-layered spectral model with application to wind-induced motion in the presence of stratification and a bottom slope', *Continental Shelf Research*, 4(3), 279–319 (1985).
10. K-T. Tee, 'The structure of three-dimensional tide-generating currents. Part I: oscillating currents', *J. Phys. Oceanography*, 9(5), 930–944 (1979).
11. D. R. Lynch and C. B. Officer, 'Analytic test cases for three-dimensional hydrodynamic models', *Int. j. numer. methods fluids*, 5, 529–543 (1985).
12. C. Le Provost, G. Rougier and A. Poncet, 'Numerical modeling of the harmonic constituents of the tides, with application to the English Channel', *J. Phys. Oceanography*, 11, 1123–1138 (1981).
13. J. J. Dongarra, 'Performance of various computers using standard linear equations software in a FORTRAN environment', *Tech. Memo. No. 23*, Mathematics & Computer Science Dept., Argonne National Laboratory, 22 April 1986.

14. D. R. Lynch and W. G. Gray, 'A wave equation model for finite element tidal computations', *Computers and Fluids*, **7**, 207–228 (1979).

15. W. G. Gray, 'On normal flow boundary conditions in finite element codes for two-dimensional shallow water flow', *Int. j. numer. methods fluids*, **4**, 99–104 (1984).

16. D. R. Lynch and W. G. Gray, 'Analytic solutions for computer flow model testing', *ASCE J. Hydraulic Division*, **104** (HY 10), 1409–1428 (1978).

17. W. G. Gray and D. R. Lynch, 'On the control of noise in finite element tidal computations', *Computers and Fluids*, **7**, 47–67 (1979).

18. G. W. Platzman, 'Some response characteristics of finite-element tidal models', *J. Comput. Phys.*, **40**(1), 36–63 (1981).

19. R. A. Walters, 'Numerically induced oscillations in finite element approximations to the shallow water equations', *Int. j. numer. methods fluids*, **3**(6), 591–604 (1983).

20. I. P. E. Kinnmark and W. G. Gray, 'A two-dimensional analysis of the wave equation model for finite element tidal computations', *Int. j. numer. methods eng.*, **20**, 369–383 (1984).

21. I. P. E. Kinnmark and W. G. Gray, 'Stability and accuracy of spatial approximations for wave equation tidal models', *J. Comput. Phys.*, **60**(3), 447–466 (1985).

22. I. P. E. Kinnmark and W. G. Gray, 'The 2Δx test: a tool for analyzing spurious oscillations', *Adv. Water Resources*, **8**, 129–135 (1985).

23. M. G. G. Foreman, 'A two-dimensional dispersion analysis of selected methods for solving the linearized shallow water equations', *J. Comput. Phys.*, **56**(2), 287–323 (1984).

24. A. C. Redfield, 'The tidal system of Lake Maracaibo, Venezuela', *Limnology and Oceanography*, **6**, 1–12 (1961).

25. J. M. Molines and M. Fornerino, 'Análisis armónico de registros de niveles. Prediccion de mareas en el Lago de Maracaibo', *Revista Técnica*, Facultad de Ingenieria, La Universidad del Zulia, 1985.

26. J. Brezina, 'Experience with a small scale, highly distorted fixed bed model of the Lake Maracaibo Estuary', *Symposium on Modelling Techniques, 2nd Annual Symp. of the Waterways, Harbors and Coastal Eng. Div. of the ASCE*, **1**, 675–689 (1975).

27. G. Parra-Pardi, *et al. Estudio Integral sobre la contaminación del Lago de Maracaibo y sus Afluentes, Partes I & II*, Ministerio del Ambiente y de los Recursos Naturales Renovables, Caracas, Venezuela, 1979.

28. J. M. Zeigler, 'The hydrography and sediments of the Gulf of Venezuela', *Limnology and Oceanography*, **9**, 397–411 (1964).